NASA Contractor Report 191490

DOPPLER GLOBAL VELOCIMETRY

DEVELOPMENT OF A FLIGHT RESEARCH INSTRUMENTATION SYSTEM FOR APPLICATION TO NON-INTRUSIVE MEASUREMENTS OF THE FLOW FIELD

Hiroshi Komine, Stephen J. Brosnan, William H. Long,
and Eddy A. Stappaerts

Northrop Corporation
Electronics Systems Division
Hawthorne, California

Contract NAS1-19940
26 January 1994

National Aeronautics and
Space Administration

Langley Research Center
Hampton, Virginia 23681-0001

NORTHROP
Electronics Systems Division
Northrop Corporation
2301 West 120th Street
P.O. Box 5032
Hawthorne, California 90251-5032
Telephone (213) 600-3000

CONTRACT DATA REQUIREMENT

CONTRACT NO. NAS1-19940

PROGRAM NAME: DOPPLER GLOBAL VOCIMETRY

CDRL TITLE: DOPPLER GLOBAL VOCIMETRY - FINAL REPORT

CDRL NO: DRL-12 S.O.W.

DOCUMENT TITLE: DEVELOPMENT OF A FLIGHT RESEARCH INSTRUMENTATION SYSTEM FOR APPLICATION TO NON- INTRUSIVE MEASUREMENTS OF THE FLOW FIELD.

DOCUMENT DATE:

PREPARED BY: LASERS AND OPTICS ENGINEERING
ORGANIZATION NAME

LM20/A8 (213) 600-3503
ORGN. NO. AND TELEPHONE NO.

— INTERNAL ONLY
— INFORMATION SUBMITTAL
— SUBMITTAL FOR APPROVAL*
X APPROVED SUBMITTAL
*APPROVAL IDENT. 126/LJT (NAS1-19440)

NORTHROP FILE NUMBER

94- 26468

Table of Contents

1.0 OVERVIEW

Doppler global velocimetry (DGV) offers a new diagnostic tool for flow field measurements[1-4]. Unlike previously developed techniques, DGV has the potential for acquiring quantitative velocity data during flight maneuvers. This capability, if realized, would represent a major advance in flight testing. The application of DGV in wind tunnel measurements, for subsonic to hypersonic speeds, would also represent a major new capability.

A key objective of the base period of the Northrop/NASA DGV program was to evaluate the feasibility of a flight system for use in NASA's High Angle-of-attack Research Vehicle (HARV) program. Figure 1-1 shows the locations of measurement planes between HARV stations 440 and 524. The objective is to obtain velocity data for vortical flow fields over a 2 meter by 2 meter region above the wing. The desired measurement accuracy is 7%, with a spatial resolution of 1 cm. The measurements would be carried out at angle-of-attack up to 50 degrees.

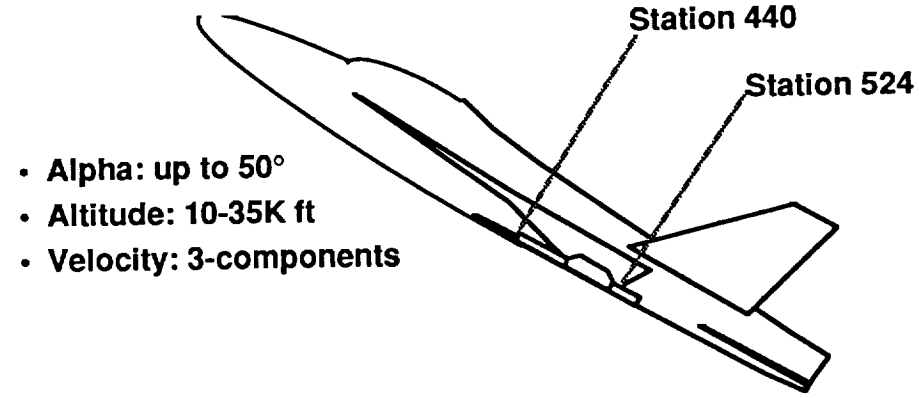

Figure 1-1 Test Conditions for F-18 HARV DGV Experiment

The first phase of the DGV program has addressed the feasibility of such a system. In particular, measurement errors, DGV hardware issues, and system installation issues have been addressed. The result is a solid basis which can be used for further system development.

Demonstrating the accuracy of the DGV technique has been another major objective of the base period effort. Calibration and error analysis of a laboratory DGV system based on a frequency-doubled Nd:YAG laser and an iodine absorption line filter (ALF) have been carried out. The test results show excellent agreement between DGV data and pitot probe measurements on a laminar flow jet with velocities of up to 150 meters per second. Camera noise was found to be the primary error source, but data with good signal-to-noise ratios were obtained at optimized light-sheet intensities and seeding levels.

As part of this program we also surveyed key DGV system components relevant to the flight system, including lasers, absorption line filters (ALFs), and cameras. Nd:host lasers and iodine ALFs were found to represent the most mature laser and filter candidates for flight and wind tunnel systems. Cameras with electronic shutters were shown to suppress solar background to an acceptable level.

In summary, the accomplishments of the base period have provided a solid foundation for further development of the DGV system.

2.0 INTRODUCTION AND BACKGROUND

Doppler Global Velocimetry (DGV)

In this section, we describe a novel subsonic/supersonic velocimetry technique that was invented and under development at Northrop since 1985. This technique permits quantitative visualization of flow field velocity profiles of unsteady phenomena, such as vortices, cavity effects, and jet mixing. This technique is referred to as Doppler Global Velocimetry because of its ability to measure global velocity components from Doppler frequency shifts. Our DGV measurements on a free-expansion air-jet at subsonic velocities and NASA's DGV experiments on vortex flows in the BART facility at Langley Research Center have validated the DGV concept for flow field diagnostics.

PRINCIPLE OF OPERATION

The basic concept of our velocimetry technique involves a method of sensing seeded flow fields illuminated by a laser light-sheet. An optical receiver images the Doppler-shifted scattered light and converts the amount of Doppler-shift into intensity variations. In contrast to conventional light-sheet visualization methods, these Doppler images yield *quantitative* measurements of the flow velocities. Three velocity vector components describing the complete vector field are obtained by taking three simultaneous images at different observation directions of the receivers.

The Doppler frequency shift, $\Delta\nu$, due to scattering from particles moving at velocity $\mathbf{v}$ is determined by the observer direction and laser beam direction according to:

$$\Delta\nu=\nu_o(\mathbf{o} - \mathbf{i}) \cdot \mathbf{v} /c$$

where c is the speed of light, ν_o is the laser frequency, and $\mathbf{o}$ and $\mathbf{i}$ are unit vectors along the observer and laser beam directions, respectively. For three-component velocimetry, two generic configuration geometries are possible. One configuration uses three observer directions ($\mathbf{o}_1$, $\mathbf{o}_2$, $\mathbf{o}_3$) and a single laser ($\mathbf{i}_0$) light-sheet. Another configuration uses three laser light-sheets ($\mathbf{i}_1$, $\mathbf{i}_2$, $\mathbf{i}_3$) and a single observer direction ($\mathbf{o}_0$).

Two distinct modes of operation are possible, depending on the type of illuminating laser. In the first scheme, a CW laser is used, and scattered light is collected during an entire camera frame time (typically 30 frames/sec). This mode of operation is limited to flows which are varying slowly (compared to this relatively long averaging period). In the second scheme, a pulsed laser with a pulse length on the order of ten nanoseconds provides the illumination. In this case, the flow is effectively frozen, and this pulsed technique provides accurate results even for flows which are changing very rapidly. Therefore, the DGV technique provides a new capability for real-time, three-component velocimetry of unsteady flows, which can not be handled by conventional LDV methods. Furthermore, 3-D global velocimetry is possible by moving the laser light-sheet to different cross sections of the flow.

The images collected by the cameras are digitized and stored in a computer for further processing. Figure 2-1 illustrates a block diagram of a configuration based on one laser light-sheet and three Doppler image receiver units.

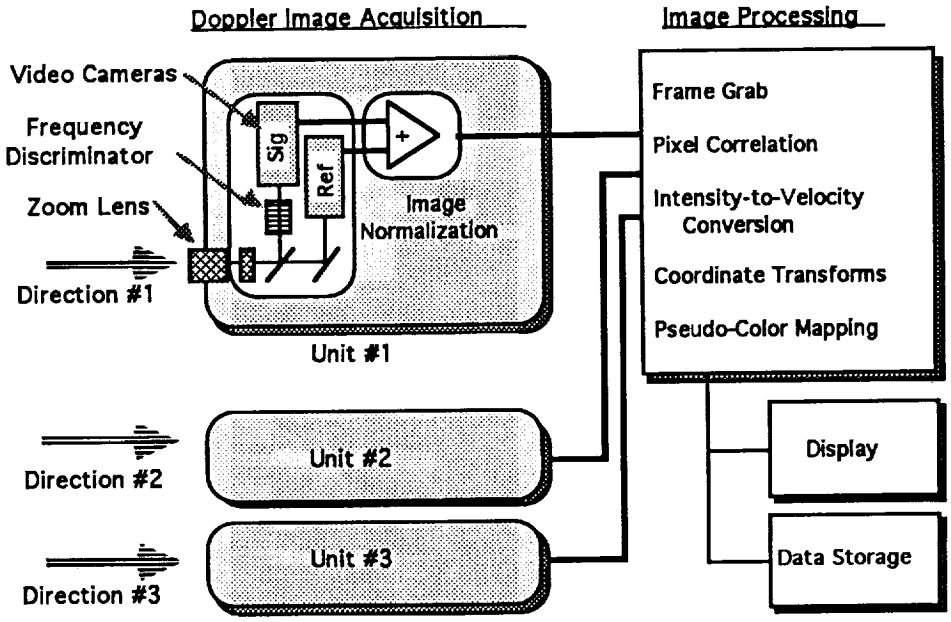

Figure 2-1 Doppler image acquisition and processing block diagram

First, for each unit, a Doppler image is obtained by a video camera that looks through a frequency discriminator whose transmission varies with frequency shift. This filtered Doppler image is normalized to a reference image of the same scene obtained without a discriminator in order to eliminate the effect of illumination and particle density nonuniformities. Next, simultaneous images from three observation directions are used to compute the three velocity components for each point of the flow cross section. Finally, the reduced data can be displayed graphically to complete the visualization process.

The DGV concept assumes that the seed particles represent the motion of the flow. The particle size distribution must be controlled to ensure this condition.

A laser light-sheet illuminates a cross section of the flow, thereby creating a thin, planar region of light scattering by the seed particles. The light scattered by the moving seed particles is shifted in frequency by the Doppler effect. In the analyzer plane, an image is produced that contains the Doppler-shift information at each "point" in the illuminated plane of the flow. This point is actually a small volume whose dimensions are determined by the light-sheet thickness and the image resolution of the camera. Each of these volume elements contains aggregates of particles that contribute to the scattering. Our velocimetry technique measures the ensemble average of the motion of the seed particles within each volume element. It is important that the seed particle number density is sufficiently low to eliminate multiple scattering.

The image detection is carried out simultaneously throughout the observed region of the illuminated plane. We can vary the size of the observed region and the spatial resolution proportionately by using various telephoto lenses on the camera. This allows the study of flow features at different scale sizes.

The conversion of the Doppler-shifted light into image intensity variations utilizes an optical frequency discriminator whose transmission varies as a function of frequency. The analyzed image intensity at each point varies according to the local Doppler-shifted frequency. In contrast to molecular Rayleigh scattering in which the Doppler shifted light exhibits a relatively broad spectrum due to thermal broadening[5], particle (Mie) scattering does not appreciably broaden the laser spectrum.

The key element of this optical frequency discriminator is an absorption line filter (ALF). The ALF cell contains atoms or molecules with an absorption line near the laser frequency. The laser frequency is tuned to one side of the absorption line profile where the absorption changes approximately linearly with frequency . Figure 2-2 shows a representative cell transmission spectrum of an ALF centered at a frequency ν_a.

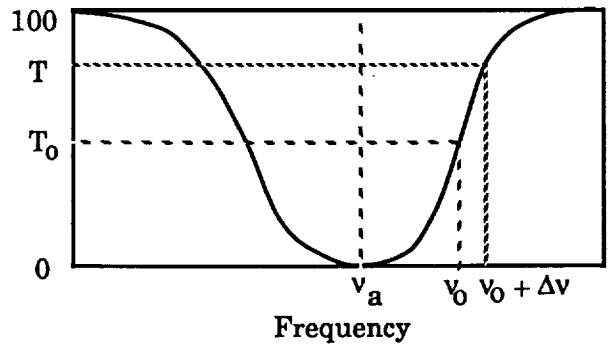

Figure 2-2 Transmission curve vs. frequency of scattered light.

The laser frequency bandwidth must be much narrower than the width of the absorption profile. In Figure 2-2, the laser center frequency (ν_0) is tuned to yield a nominal transmission (T_0) near 50% on the high frequency side of the absorption profile. In general, a small bandwidth about the center frequency results in an average transmission value which depends on the absorption profile and the laser spectrum.

The operating point takes into account the Doppler shift due to the free-stream flow velocity. Doppler-shifted frequencies ($\nu_0 + \Delta\nu$) higher than that of the free-stream value will result in increased transmission (T), while the opposite is true if the Doppler shift yields lower frequencies. The dependence of transmission on frequency can be reversed by tuning the laser to the lower frequency side of the absorption profile.

Molecular iodine and bromine vapor as well as alkali (cesium Cs and rubidium Rb) vapors are some of the candidates for absorption media. These atoms and molecules have many absorption lines that match visible and near-infrared laser frequencies. For example, the argon-ion laser emission at 514.5 nm can be tuned to an iodine absorption line, while frequency-doubled neodymium lasers provide a match in both iodine and bromine. The Ti:sapphire laser and semiconductor diode lasers can be tuned to Cs and Rb resonance lines.

Figure 2-3 shows a transmission profile of an iodine cell near 514.5nm. If the laser frequency is tuned to yield approximately 50% transmission on the high frequency side of the absorption wing, a Doppler shift of 100 MHz, corresponding to a velocity component of 51.5 m/sec, yields a transmission change of about 15%.

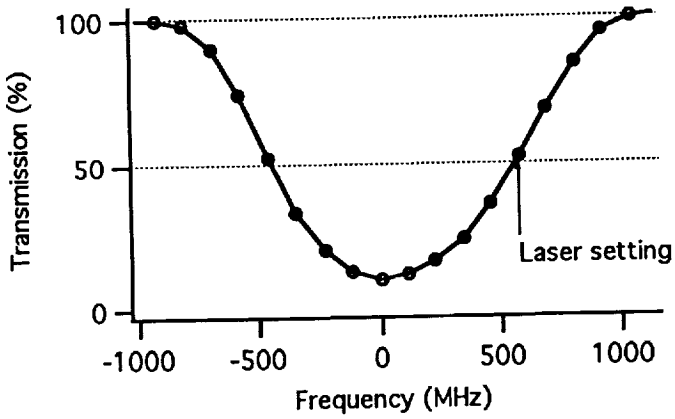

Figure 2-3 Iodine cell transmission vs. frequency near 514.5 nm

The approximately linear portion of the absorption profile spans an operating frequency range of about 600 MHz. For larger velocity changes, buffer gas can be added to the molecular vapor cell; this will broaden the absorption line width and increase the frequency range.

The discussions so far assumed that both the laser illumination and the scatterer density in the flow were uniform. This will usually not be the case, and the nonuniformities must be taken into account in the image processing. Our solution is to normalize the transmitted image through the ALF cell to an identical image obtained without a cell. This is achieved by using two identical cameras and a beam splitter, as schematically shown in Figure 2-4.

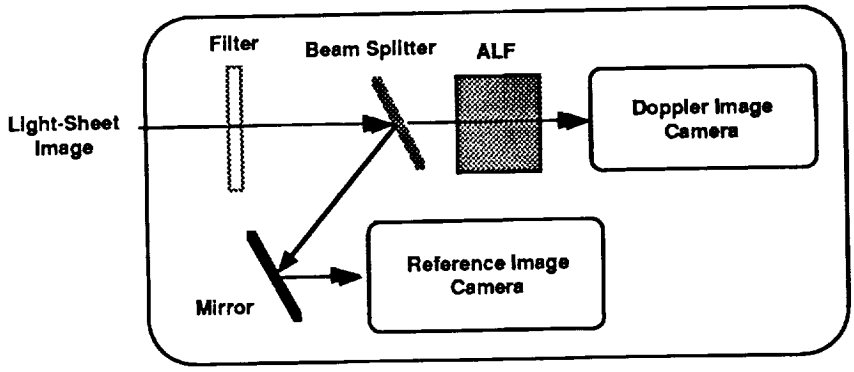

Figure 2-4: Optical schematic diagram of Doppler image normalization

The beam splitter must be insensitive to the polarization of the scattered light. This is an important optical design feature because light scattering from (micron-sized) seed particles exhibits strong polarization dependence on observer direction and light-sheet polarization.

The DGV image processing uses a two-step algorithm to transform the Doppler images into velocity data. The first step determines the observation directions of the three Doppler image receivers and the physical dimensions of the region seen by these units. This step is performed once for a particular measurement geometry prior to Doppler image acquisition. The second step calculates the orthogonal velocity components at each sample point in the illuminated plane from a set of three normalized Doppler images. The latter step is repeated for each set of snapshot images.

The snapshots can be accumulated to construct an equivalent of time-averaged data; this procedure permits a direct comparison with other steady-state measurement methods. As discussed in the next section, a comparison with pitot probe scan data provides a means of evaluating the accuracy of the DGV measurements. Once the accuracy is quantified, these DGV snapshots offer a new way to look at flow dynamics.

3.0 PROGRAM OBJECTIVES AND ACCOMPLISHMENTS

3.1 DGV System Calibration and Error Analysis

The DGV system calibration test was carried out by conducting a one-component DGV measurement on a seeded laminar-flow subsonic jet that had been used at the Northrop Aircraft Division for calibrating pitot sensors. Below we describe the laser lightsheet source, the receiver, the seeded jet, and the measurement results.

3.1.1 Pulsed Nd:YAG/SHG laser system

A successful DGV implementation requires a narrowband frequency-stable laser source that can be frequency-locked to the side of an ALF filter absorption line. A block diagram is shown in Figure 3.1-1. We used an injection-seeded lamp-pumped Nd:YAG oscillator/amplifier that was locked to a single axial mode and was tuned by temperature adjustment of the seed laser. The frequency was determined from a transmission measurement of a duplicate ALF cell.

The seed laser was a Lightwave Electronics S100-02. This model uses a feedback loop to maintain its slave laser in a single axial mode, and it included a factory option to allow the laser crystal temperature (and consequently the laser frequency) to be adjusted by the input of a control voltage.

The seed laser controller maintained the slave laser in a single axial mode. The buildup time of the slave oscillator was minimized by adjusting its cavity length with a piezoelectric transducer to match the seed laser's frequency. The slave laser's frequency was dithered by ±5 MHz by varying its cavity length. The control loop acted to match the buildup time for opposing sides of the optimum cavity spacing. This dither was a concern for the DGV measurement, and it made necessary an ALF transmission measurement on each laser pulse. The seed laser output was then mode-matched for best locking into the slave oscillator using a lens and two steering mirrors using standard techniques.

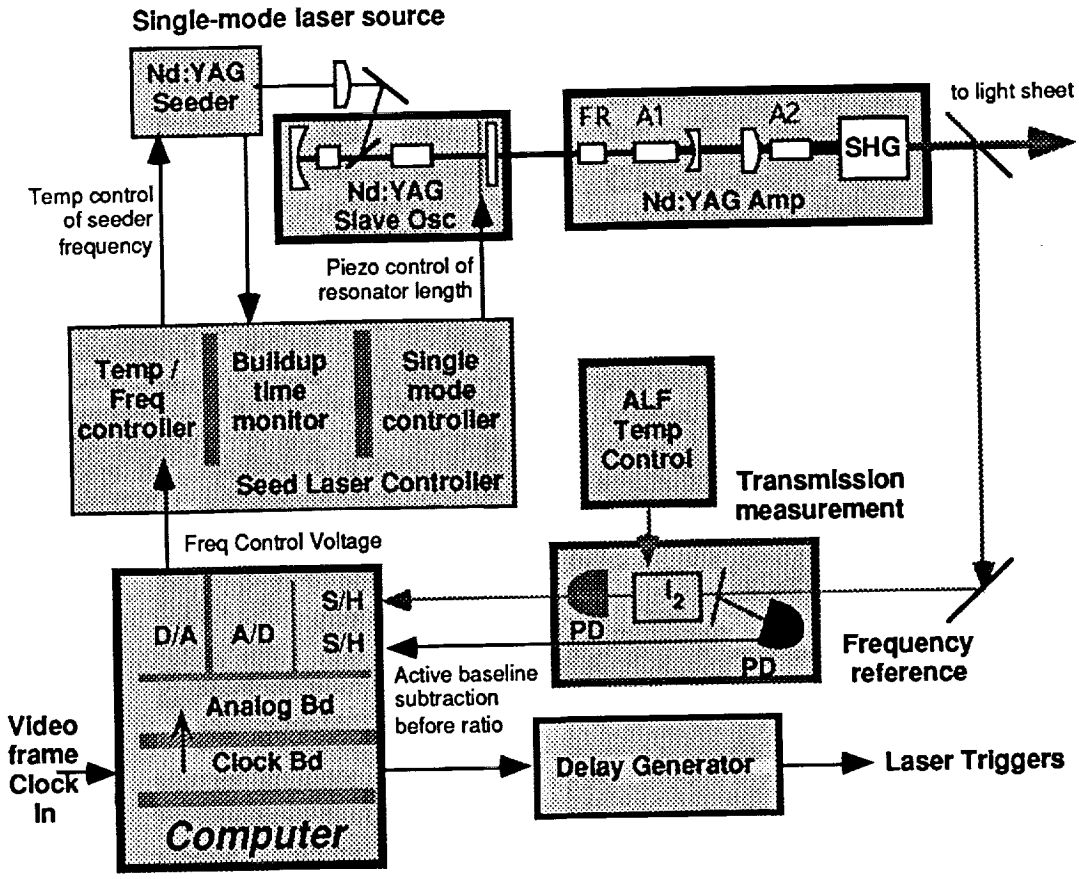

Figure 3.1-1: DGV laser transmitter setup with frequency control.

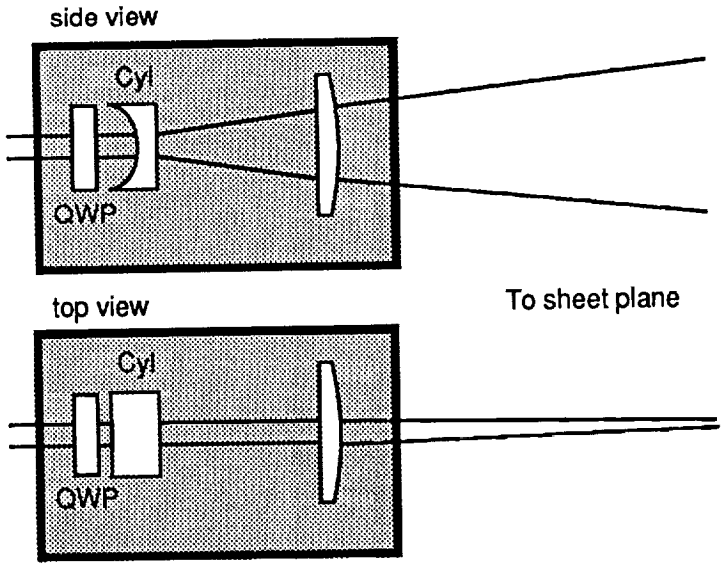

The slave oscillator was a SpectraPhysics DCR-11 Nd:YAG laser which was customized to be a TEM_{00} oscillator in which the seed radiation was coupled into the cavity at the Q-switch polarizer. The laser was run at a low power setting (23-24 J into the flashlamps) in order to yield a longer pulse, approximately 20 ns. The slave laser pulse energy was approximately 4 mJ and was directed into the two stage power amplifier.

The amplifier was a substantially modified Quantel Model YG660 Nd:YAG laser. The oscillator optics were removed and the laser was reconfigured to be a two-stage amplifier. An Optics-For-Research Faraday isolator was used at the entrance to protect the slave oscillator from optical feedback. A telescope between the two amplifier sections was adjusted to compensate for thermal focussing so that the laser output was collimated at operating power. The infrared beam was then frequency doubled into the green with the unit's existing harmonic generator. The remaining infrared light was separated with dichroic beamsplitters (not shown) and discarded. The visible beam of 20 mJ at 532 nm was then directed to the diagnostics and lightsheet shaping optics.

Frequency diagnostics included a 15 cm Fabry-Perot etalon with ring-pattern video monitor and the ALF transmission sensor. This sensor consisted of a duplicate ALF cell, a pair of photodiodes (ThorLabs DET1-Si), and a 50% beamsplitter. The reference photodiode received its signal from the beamsplitter reflection. The angle of incidence was minimized ($< 5°$) to minimize any polarization effects. The signal photodiode was illuminated through the ALF.

The electrical signals from the detectors were terminated with high impedance, so the waveforms exhibited a long RC-decay tail. The peaks of the signals were captured by simultaneous sample-and-hold circuits on a PC-mounted card (Data Translation DT2828). Some signal baseline variation was observed, perhaps due to 60-cycle noise pickup over the long cable lengths, and resulted in reference cell transmission measurement errors. This problem was eliminated by sampling the signal and reference photodiode waveforms before and after the laser pulse. The baselines were then subtracted prior to ratioing. The timing signals necessary for this operation were provided by another PC-mounted card (DT2819).

The clock source for the timing card was derived from the video frame vertical sync, a 30 Hz clock provided by a master composite-video sync module, constructed by Northrop for prior IR&D programs. A 10 Hz laser trigger clock was derived from the same 30 Hz source. In addition, the RS–170 master composite video sync was routed to all receiver cameras, which were run in genlocked mode (an option that enables a external synchronization).

The frequency locking control loop consisted of the ALF transmission sensor, the frequency control computer, and the seed-laser temperature control. The computer captured the voltage samples with the analog board, computed the baseline-compensated transmission, judged whether a laser correction was necessary, and if so sent a control voltage to the seed-laser controller. The controller's function was to maintain a constant ALF transmission. In

addition, the computer supplied a synchronized transmission measurement to the image acquisition computer for each acquired image set via a serial link between the computers.

The lightsheet shaping optics consisted of a beam shaping telescope, a quarter wave plate, and beam steering mirrors (Figure 3.1-2). The round 6-mm-diameter input beam was first expanded in one dimension by a short-focal-length negative cylindrical lens. After sufficient expansion, a long-focal-length positive spherical lens was used both to reduce the expansion (or collimate) in the first direction and also to focus the beam in the other direction to a minimum line thickness at the desired lightsheet location. The focal length selection and spacing of the lenses determined the fan angle of the sheet. This must be tailored to the particular flow under study.

The quarter-wave plate was used to give the transmitted beam a rotating polarization vector. This acted to reduce the polarization sensitivity of the receiver's beamsplitter (see below) since all polarizations are averaged over each optical cycle. At Northrop's suggestion, this technique was successfully used during the BART wind tunnel test at NASA Langley[6] during the course of the contract period.

3.1.2 DGV Receiver

The DGV receiver gathered the Doppler-shifted light scattered from seed particles flowing through the light sheet and converted it into useful velocity information. It consisted of a pair of video cameras that were carefully adjusted to provide pixel-by-pixel alignment over the area of the laser light sheet. One camera observed the scene through the ALF and the other observed the scene directly. The ALF impressed an intensity-modulated velocity map upon the light-sheet scene. The second camera provided a reference image, so that a ratio of the two cameras produced an image that had only velocity information.

The receiver subsystem consisted of two CCD video cameras, an optical train, and a temperature-controlled ALF cell.

The cameras were Cohu Model 4810, incorporating an interline readout CCD with 754(H)x488(V) elements in a 8.8x6.6 mm format. Output was normal 2:1 interlaced RS-170. The cameras were fitted with f/1.4 50 mm lenses and were genlocked to a master video composite sync signal. Test results of cameras considered for the next phase of the DGV program are described in Section 3.2.1.

An idiosyncrasy of the camera sensor was revealed when pulsed laser illumination was used. Only one video field had an image. Apparently the Texas Instruments sensor gathers light only one field at a time, so when the laser was pulsed at the top of the even video field, there was no signal in the odd field.

The boresight optical arrangement used for the calibration test is shown in Figure 3.1-3. The two cameras were aligned so that they were both directed down a common axis and also

overlapped pixel by pixel. Camera adjustments that were necessary to produce boresighted pixel alignment included:

(1) Tilt adjustments of the beamsplitter and steering mirrors. The reference camera arm was aligned down the boresight (the axis defined by the ALF camera pointing direction) by adjustment of the beamsplitter and steering mirrors.
(2) Axial translation of one camera to match path lengths from the cameras to the beamsplitter. This was required for matching magnification. The tolerance allowed was approximately 1 mm.
(3) Camera focussing. There was crosstalk between focussing and path matching.
(4) Rotation of the ALF camera about its axis. If the cameras were at unequal height, the tilt adjustments (1) produced an effective rotation of the reference image. Rotation of one camera with approximately 0.5 milliradian angular tolerance was then required.

A 10-nm-passband 532 nm interference filter was placed in front of the beamsplitter to reduce the effect of ambient light. Background elimination is discussed further in Section 3.2.1.

The presence of a tilted beamsplitter flat produced astigmatism in the ALF camera image. To compensate for this error, we reversed the direction of the beamsplitter so that the reference image traversed the beamsplitter twice, and introduced a compensation plate of equal thickness behind the beamsplitter. Both the ALF and reference images then traversed a tilted plate of equal optical thickness. The astigmatism was not removed, but both images were made to have equivalent astigmatism; pixel alignment for the ratio was thereby preserved. A genuine astigmatic corrector plate could have been incorporated behind the beamsplitter, but the added optical length required, given the existing lens focal lengths and field-of-view, made this choice undesirable.

The ALF cell, purchased complete from Opthos Instruments per Northrop specifications, was evacuated and loaded with an ample amount of solid iodine. When the cell was heated, sufficient molecular iodine vapor was produced for the filter to function. The cell subsystem shown in Figure 3.1-4 consisted of the following components:

(1) A fused silica cylinder body, 2 inch OD, with optically contacted fused silica windows. The 1/4 inch thick windows were uncoated and unwedged.
(2) Heater wire wrapped around the body near the windows, which were therefore warmer than the cell body and prevented condensation of iodine on the windows.
(3) An RTD temperature sensor contacted near the middle of the body served as the temperature controller sensor.
(4) A plastic housing with windows that enclosed the entire assembly for thermal isolation.
(5) A temperature controller (Omega CN9000A). Temperature fluctuations were limited to ±0.1°C.
(6) A variac reduced the heater voltage to a level that yielded a proportional controller duty cycle of approximately 50%.

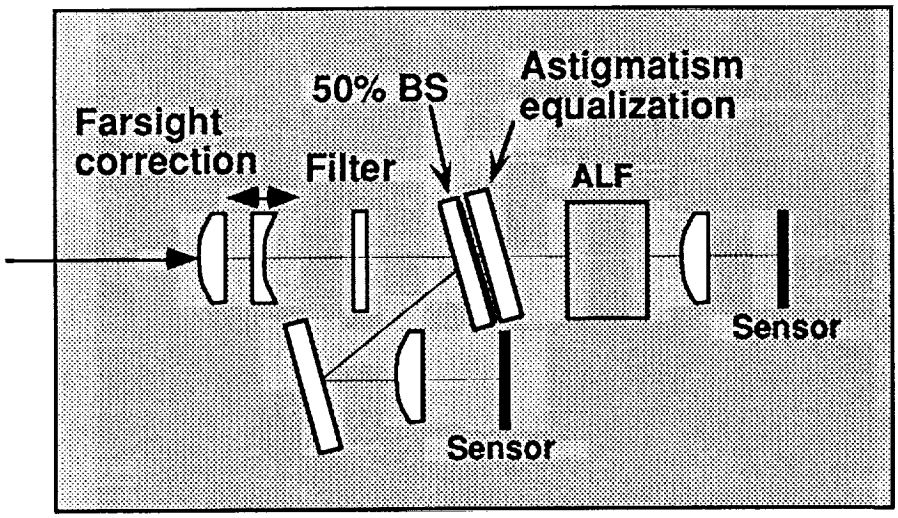

Figure 3.1-3: DGV receiver setup in boresight configuration

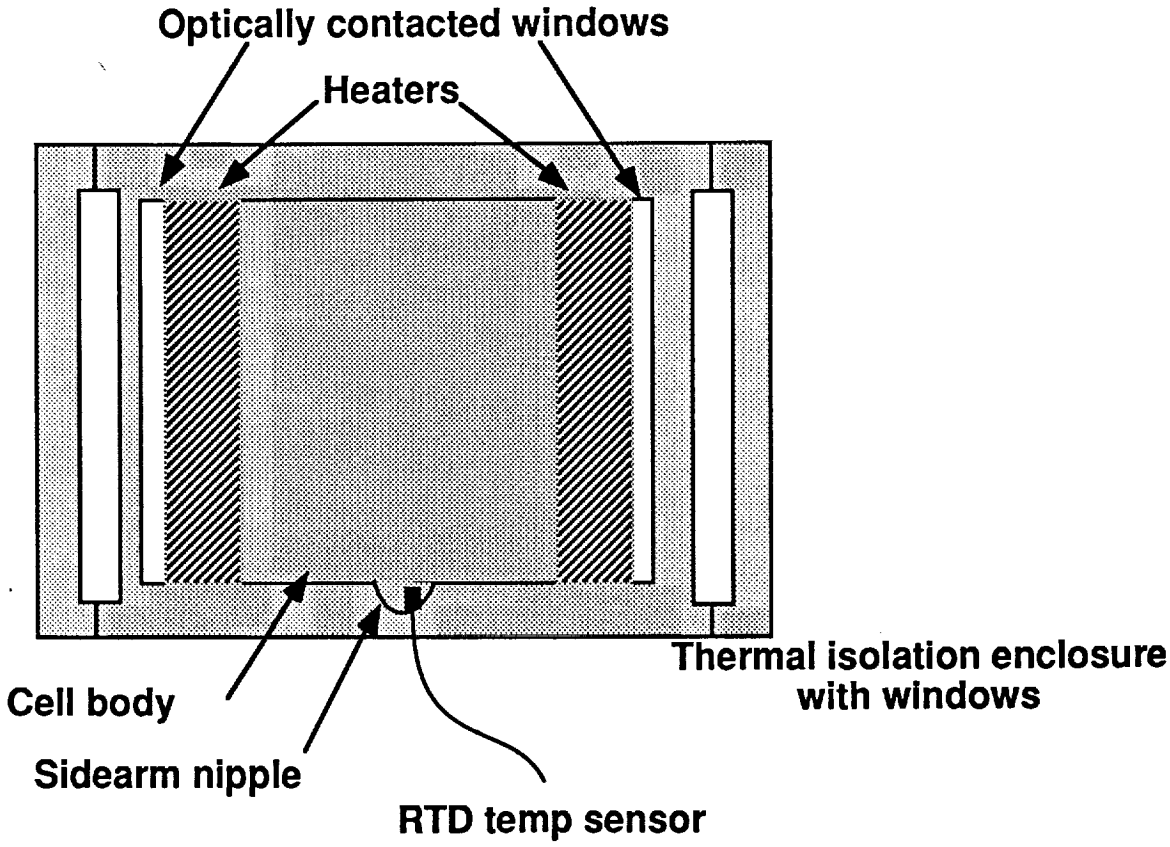

Figure 3.1-4: ALF cell design

A frequency-to-transmission characterization of the ALF was carried out prior to the DGV calibration test. This consisted essentially of a spectrographic scan of several I_2 absorption lines that lay in the injection-seeded tuning range. An example is shown in Figure 3.1-5 where the lineshape was measured versus temperature. The shape of each absorption line edge was recorded and used by the DGV image acquisition computer to convert transmission changes to velocity changes in DGV images, thereby compensating for the nonlinear response of the ALF.

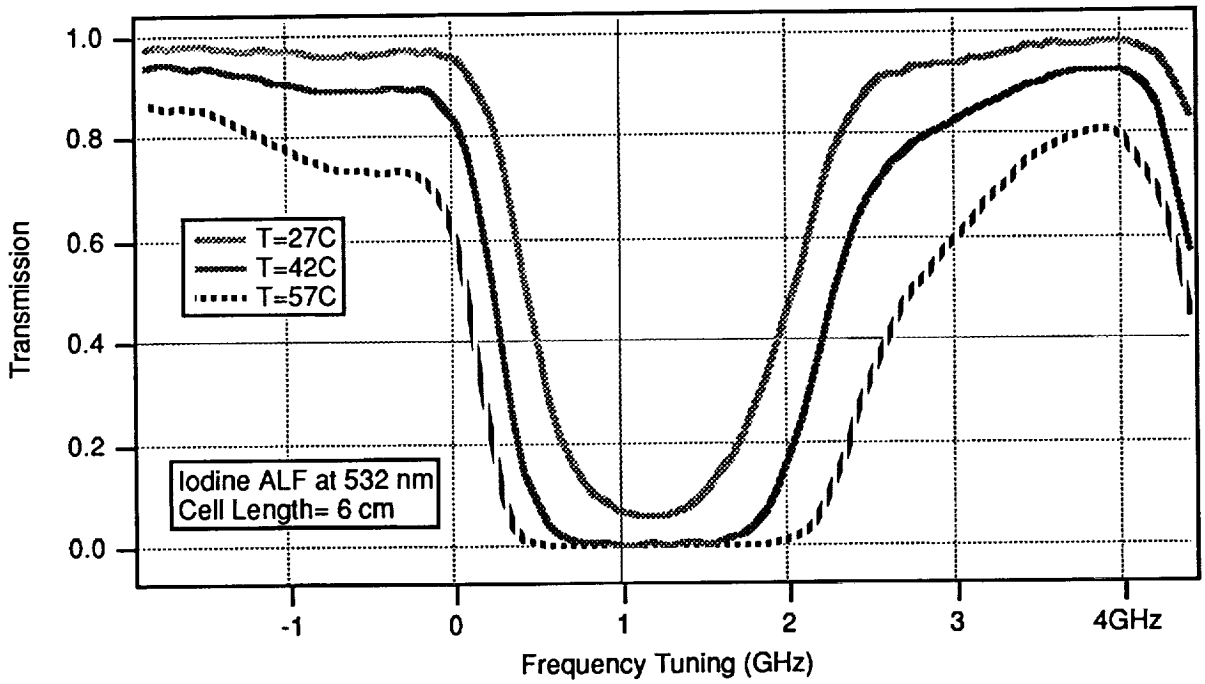

Figure 3.1-5: Iodine ALF cell transmission lineshape for three temperatures.

Since there were two ALF filters, it was important that they have the same frequency-to-transmission response. We found that small temperature offset errors could occur, perhaps due to response nonuniformity between temperature sensors. Therefore, the temperature controller set point for the receiver ALF was adjusted slightly (1-2°C) to produce transmission changes matched to that of the reference transmission cell. This matching procedure only needed to be carried out once. No daily fluctuations were observed.

3.1.3 Calibration Jet

A laminar-flow subsonic jet used at the Northrop Aircraft Division for calibrating pitot pressure probes was the airflow source for the calibration test. This device accepted pressurized air at its inlet and expanded the flow in a 2x2 feet mixing region. The flow then passed through a series of fine-mesh screens and flow straighteners several feet in length. It was then channeled through a gradual reducing section and exited at a 3x3 inch nozzle (see Figure 3.1-6). Turbulence on this device had been measured to be less than 1%.

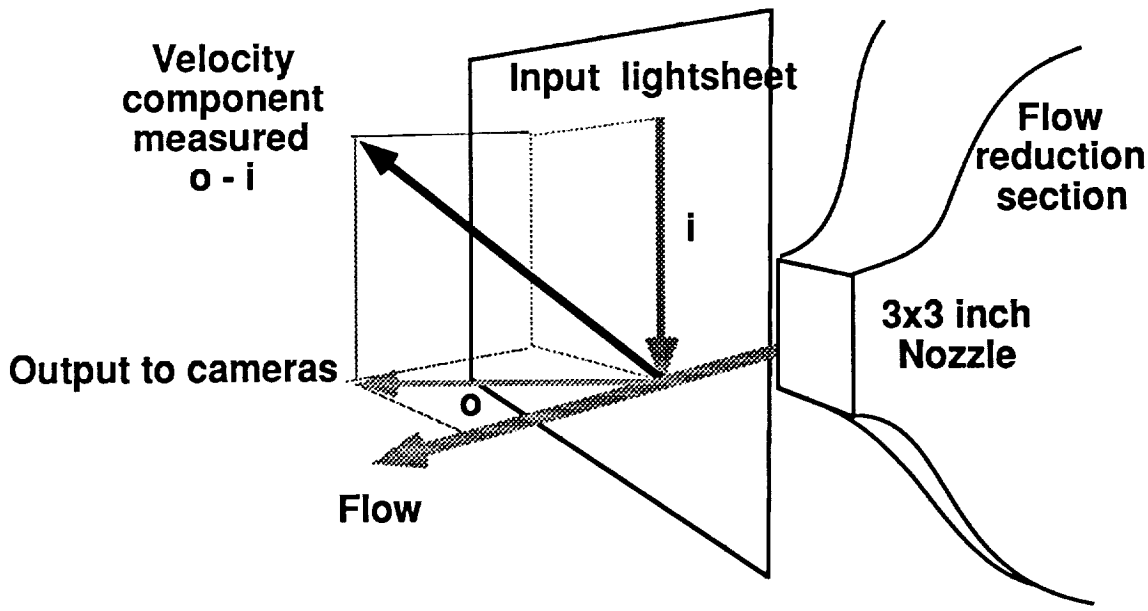

Figure 3.1-6: DGV geometry for calibration jet test.

A series of pressure probe measurements were made on the calibration jet for later comparison with DGV measurements. Probe measurements were taken streamwise every 0.2 inches across the center line of the exit nozzle in both a horizontal and vertical sweep at distances of 6", 12", and 18" back from the exit nozzle with the smoke generators off. Nominal exit velocities surveyed were 70 m/s, 100 m/s, 125 m/s, and 150 m/s. Good laminar flow velocities were measured at the 6" and 12" stations, i.e. the velocity profile was flat near the center line. At 18", the external air became entrained and the velocity profile became more bell shaped. Some asymmetry between the horizontal and vertical sweeps was observed and is not currently understood. The data gathered was repeatable and we believe it to be reliable; it is shown in the DGV comparisons described below.

An additional velocity comparison test was conducted using a commercial Laser Doppler Anemometer (LDA) device. The goal was to compare the statistical flow fluctuations that are measurable using LDA with those measured with DGV.

LDA measurements were taken using an argon ion laser operating at 514.5 nm. Measurements were taken at the same locations as for the pressure probe tests at the 6" and 12" stations. The Rosco smoke generator seed, which was injected in the tunnel mixing region for the DGV tests, proved to be unsuitable for LDA because only the excessively small particles remained after the tunnel's internal screens. The best seeding results were obtained for a water spray seed that was injected into the tunnel just prior to the nozzle exit.

The LDA data obtained showed considerable discrepancy with the pressure probe data, particularly at the 6" station. This is believed to be due to the problems associated with seeding the flow with water spray and the resulting large particle sizes For the higher speeds the large particles were unable to accelerate to the full stream velocity between the interior of

the tunnel and the survey location 6" from the nozzle. At the 12" station velocities showed less variation due to the longer distance available for the particles to accelerate.

LDA measurements of the exit nozzle velocity were considered to be unreliable due to flow seeding problems. For this reason DGV data will be compared only to pressure probe data.

Some experimentation was required to determine a suitable seeding technique. The smoke injection point was moved as far back toward the supply air as possible to maximize the seed uniformity. This was constrained by the internal pressure generated by the commercial Rosco smoke unit, which must exceed the supply air pressure at the injection point.

3.1.4 DGV Data and Analysis

Using the calibration jet, DGV velocity data were gathered to compare with pressure probe data and to ascertain relevant sources of error. The measurement geometry is shown in Figure 3.1-6. The lightsheet traversed the flow vertically from top to bottom. Since the flow was mainly horizontal, there was nominally no Doppler shift due to the input light (i.e., $\mathbf{i} \cdot \mathbf{v} = 0$). The shift measured by the receiver was mostly due to the orientation of the receiver relative to the flow.

The velocity information was computed from the ALF and reference camera images in the following way. First, since the Cohu 4810 cameras only have useful information on one video field, the missing field was synthesized by averaging the pixels directly above and below. Second, the nonuniformities due to pixel gain and fixed-pattern noise were removed for each image, as described below. Then, the ALF image was divided by the reference image to yield an ALF transmission image. Finally, the iodine lineshape data was used to derive a true DGV velocity image. The velocity component measured was that parallel to the difference between the output and input light unit wavevectors $\mathbf{o}-\mathbf{i}$.

The pixel gain correction for each camera was derived from laboratory measurements in which the response for each pixel was measured when the camera was uniformly illuminated. This uniform source was produced from a fiber-bundle-coupled tungsten lamp that was filtered to pass only green light and then apertured so as to illuminate a ground-glass scatter screen at a 50 cm range. The lensless camera was placed immediately after the scatter screen. Using the captured image, a file of 8-bit pixel-gain correction factors was created for each camera. The typical magnitude of these corrections was approximately 2-3% about the overall pixel average.

The fixed-pattern noise correction for each camera was measured just prior to each experimental run to account for variations in ambient background light, fixed scene features, as well as any fixed-pattern noise associated with the sensor. Typically, the scene with no laser illumination was averaged over 50 frames and the resulting background was saved for each camera.

The ALF filter transmission was not linear with Doppler frequency shift for high and low transmissions (see Figure 2-2). To make the processed velocity images linear with frequency shift the following procedure was applied. First, the transmission of the iodine cell was measured at frequency intervals spanning the proper absorption line. Next, an eight-bit look-up-table was constructed to map intensity-ratio pixel values to velocity pixel values using cubic spline interpolation to the lineshape data. Finally, the linearized velocity image was constructed from the look-up-table and displayed.

DGV Measurement Accuracy — The accuracy of DGV velocity measurements was tested by a comparison check with the pitot pressure probe data, using the same calibration flow jet as before, seeded with Rosco smoke generators.

A typical image set of ALF, reference, and ratio images is shown in Figure 3.1-7. Note that sharp brightness changes in the reference image did not show up in the ratio. This showed that the camera alignment was proper and that the normalization worked properly. The noise level of the ratio image was what was expected from the video noise levels of the component images. Where the reference (denominator) image was weak, noise was increased.

Significant shot-to-shot variations in both the reference and ratio images were observed, as shown in Figures 3.1.8 and 3.1.9. The reference image variations were mainly due to particle seeding fluctuations. The ratio images, from which the dependence on particle seeding variations had been removed, also showed significant differences. This is probably due to short-time-scale velocity fluctuations that were frozen by the 20 ns laser illumination strobe.

DGV images were averaged in order to compare meaningfully with the slower response pitot probe data. Both temporal averaging over several ratio images and also spatial averaging over pixel neighborhoods (convolutions) were used in the data analysis. Temporal averages were used to remove short-time-scale velocity fluctuations. Spatial averages were used to further reduce image noise and could also be used to soften the effect of small ALF camera to reference camera misalignment.

An image resulting from the average of 10 laser shots is shown in Figure 3.1-10. The variations due to short-time-scale velocity fluctuations are missing, and a more uniform image that can be compared to pitot measurements is the result. Images for the various measured flow speeds, as well as quantitative cross-sections through them including length scaling information, are shown in Figures 3.1-11 through 3.1-14. The pitot probe data is overlayed for comparison. The increased noise at the extremes of the horizontal slices were due to low light-sheet intensity at those positions at the edge of the flow.

ALF Camera

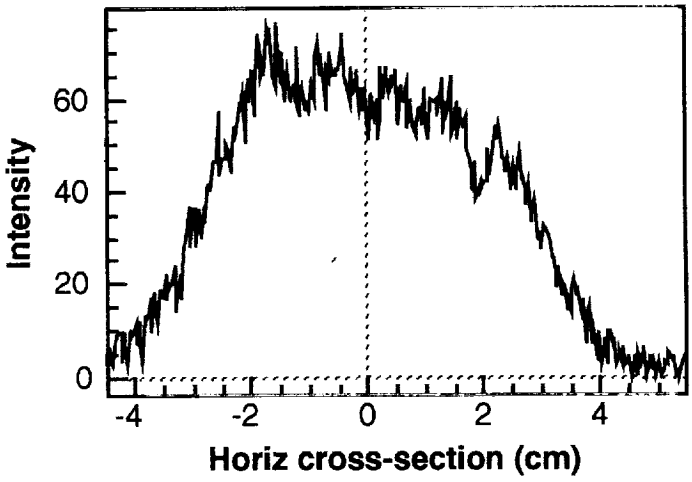

Reference Camera

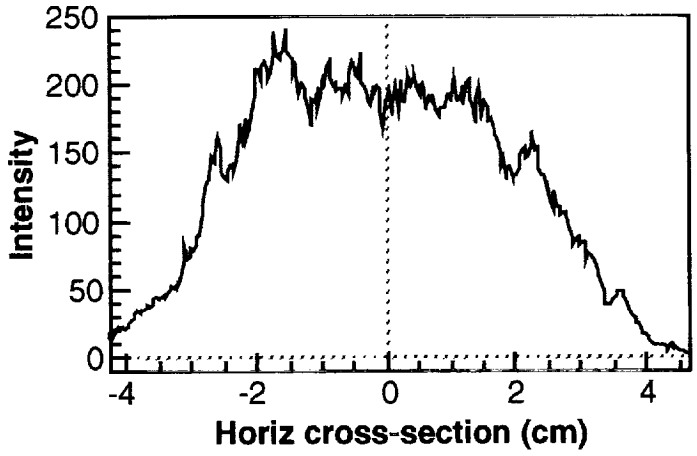

Ratio Image

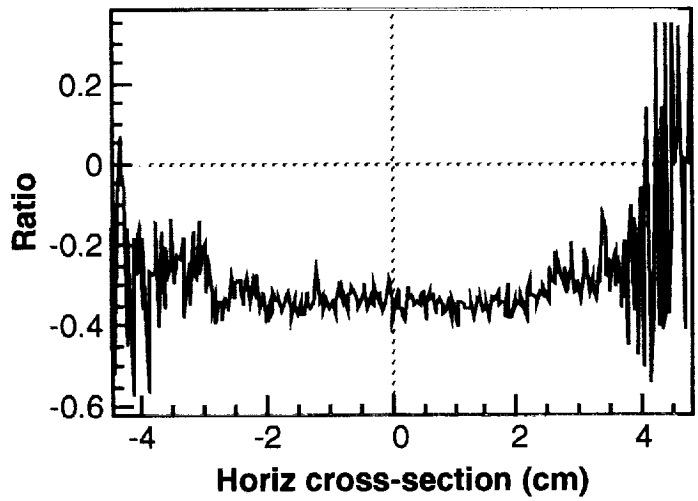

Figure 3.1.7: Sample images for a single laser shot for calibration jet plenum pressure at 2.0 psi, including horizontal cross sections taken near center of image. Note large ratio noise where reference image intensity is small.

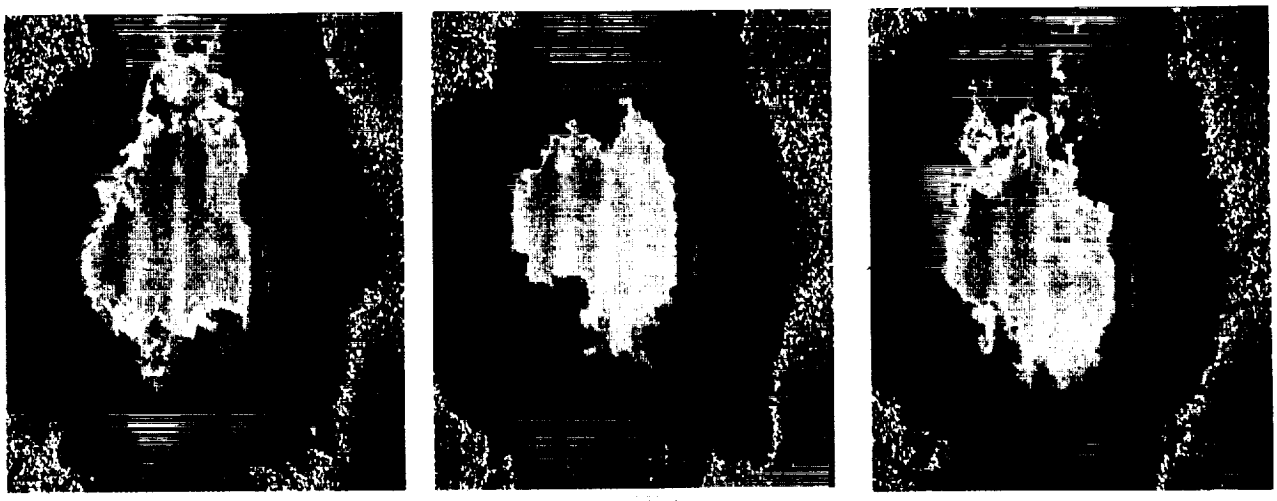

Figure 3.1-8: Shot-to-shot variation in reference image, mostly due to seed fluctuations.

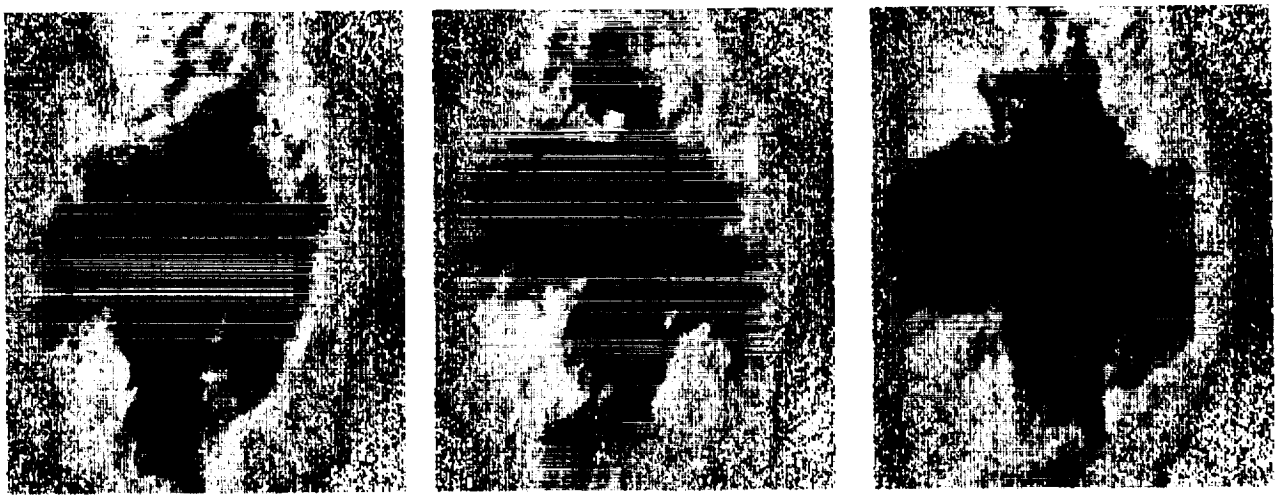

Figure 3.1-9: Shot-to-shot variation in ratio image, mostly due to short-time-scale velocity fluctuations.

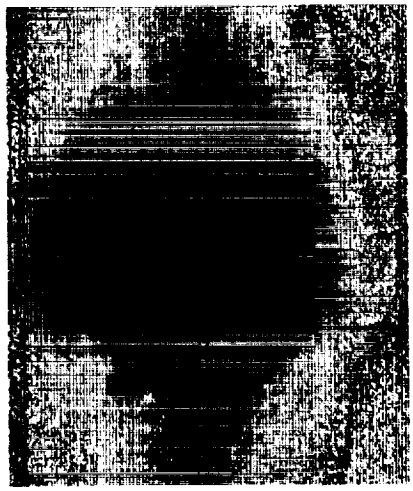

Figure 3.1-10: Average of 10 ratio images. Note that the fluctuations have been smoothed out.

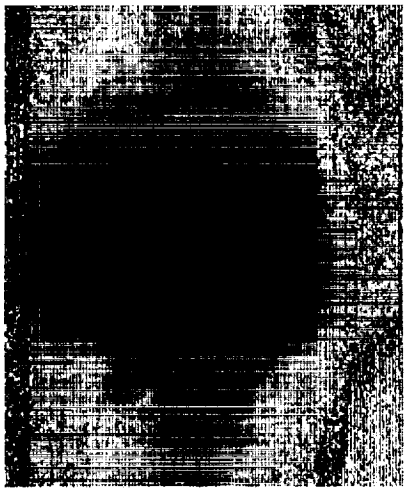

(a)

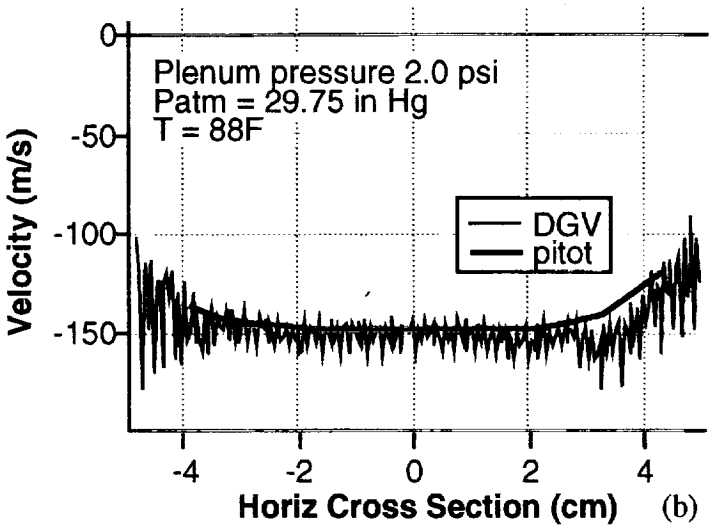

(b)

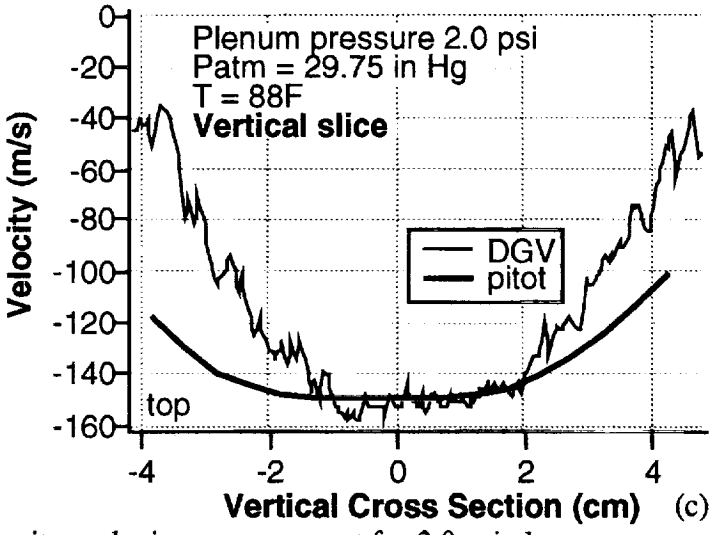

(c)

Fig 3.1-11: Comparison of DGV to pitot velocity measurement for 2.0 psi plenum pressure. (a) Ratio image. (b) Horizontal cross-section. (c) Vertical slice cross-section.

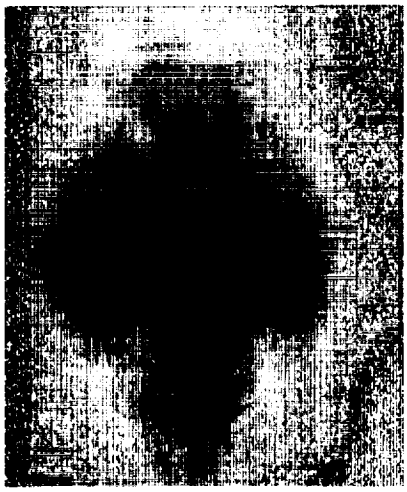

(a)

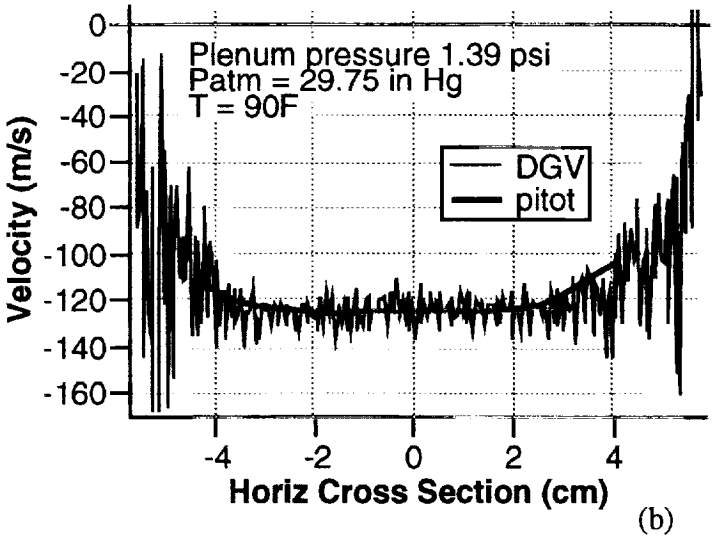

(b)

Fig 3.1-12: Comparison of DGV to pitot velocity measurement for 1.39 psi plenum pressure. (a) Ratio image. (b) Horizontal cross-section.

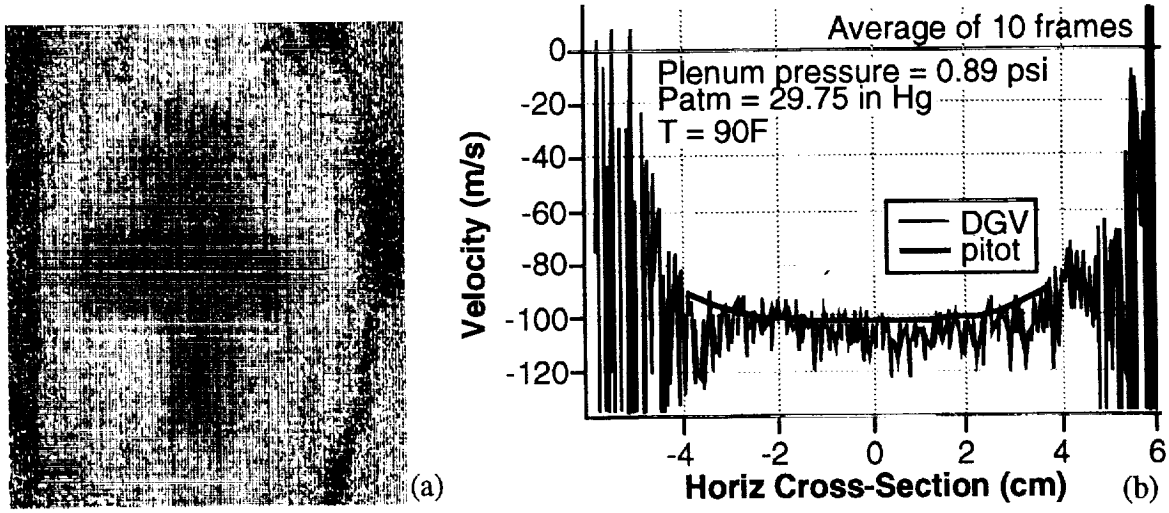

Fig. 3.1-13: Comparison of DGV to pitot velocity measurement for 0.89 psi plenum pressure (a) Ratio image. (b) Horizontal cross-section.

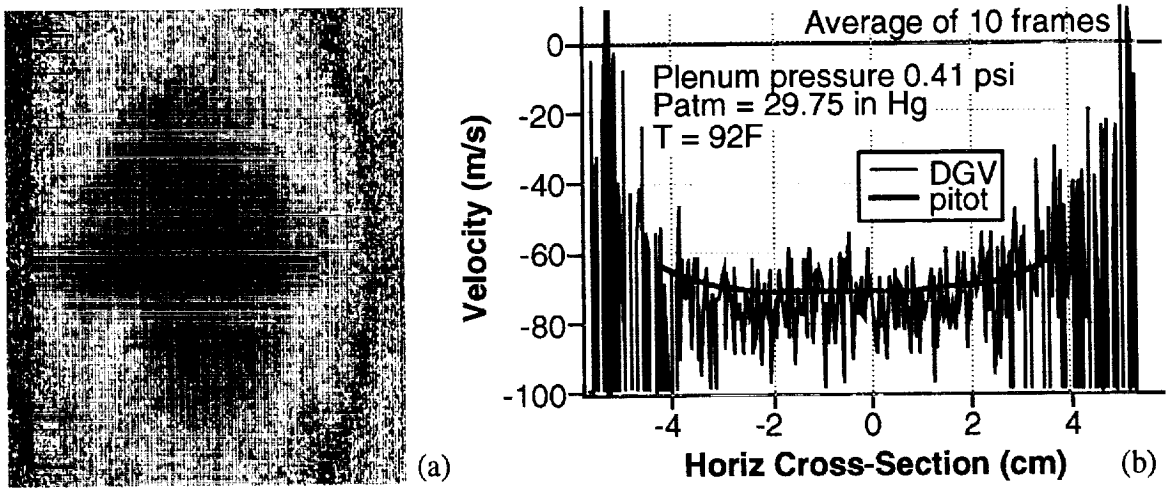

Fig. 3.1-14: Comparison of DGV to pitot velocity measurement for 0.41 psi plenum pressure (a) Ratio image. (b) Horizontal cross-section.

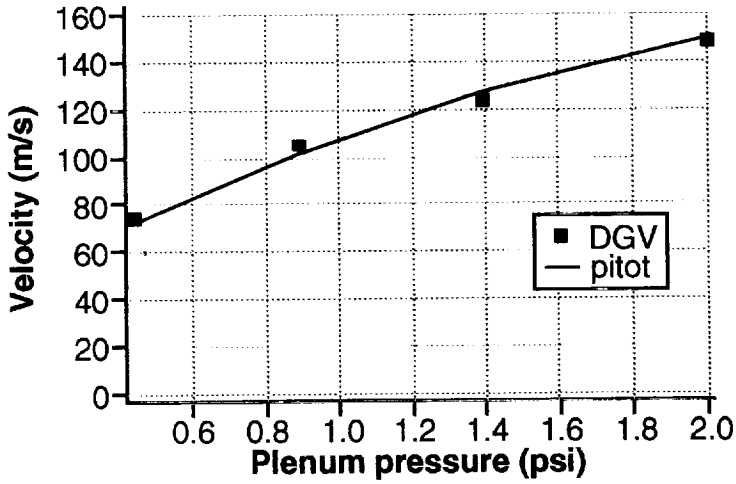

Fig. 3.1-15: Comparison of DGV to pitot velocity measurement vs plenum pressure.

A quantitative comparison of DGV versus pitot measurements at the center of the flow channel is shown in Figure 3.1-15. Since 3-D DGV measurements were not made, an assumption of unidirectional flow was made to compare with the pitot measurements. This assumption is most valid only in the center of the flow channel, where agreement was found to be good, with a maximum discrepancy of 4%.

For points away from the flow centerline, where the unidirectional flow assumption may be invalid, some deviations from the pitot measurements were observed. In particular, vertical displacements from the centerline (see Fig. 3.1-11c) showed velocity deviations of up to 50% at the edges of the 3x3 inch flow channel. Horizontal displacements showed no such anomalies.

For a lightsheet input in the -y direction and flow in the +z direction and observation from a nominal angle of 45° in the xz plane, the Doppler shift is given by

$$\Delta\nu = \lambda\left[\frac{1}{\sqrt{2}}\left(-v_x + v_z\right) + v_y\right]$$

If the non-streamwise flow was radially diverging as from an expanding jet, then both the horizontal and vertical slices should have exhibited a skewed asymmetry about the streamwise speed value. One could then argue that the finite angular acceptance of the pitot probe would account for the discrepancy from the DGV measurement. This is, however, not consistent with our measurements. It should be noted, however, that significant horizontal to vertical asymmetry in the pitot probe measurements surprised the Northrop Aircraft engineers that conducted the pitot tests. There is the possibility that the DGV measurements were more sensitive to non-streamwise flow. Only a 3-D measurement can answer that question.

The short-time-scale velocity fluctuations were measured from the pixel-by-pixel standard deviation of an averaged image data set. The result was 30 m/s out of a centerline speed of 150 m/s, as compared with a nominal 1% turbulence that was measured in the past for this calibration jet using the slower response pitot probe. No known DGV error can explain this difference. It is possible that the fast strobe feature of the DGV technique is revealing new phenomena.

DGV Measurement Noise – The primary noise sources for DGV velocity measurements have been identified and quantified. With sufficient care, noise due camera misalignment was minimized. The dominant noise was traceable to video sensor noise and could be reduced with temporal and spatial averaging.

The dominant source of DGV noise was investigated by considering a cross-section of a ratio image in which the effect of varying denominator amplitude was removed as shown in Figure 3.1-16. A smoothed version of the waveform was subtracted from the original ratio, resulting in the light trace. This was then multiplied by a smoothed copy of the denominator, and resulted in a compensated noise waveform (the solid trace) that had constant amplitude

excursion over the cross-section. The standard deviation of the compensated noise was 3.2 gray-scales. The RMS video noise of the individual numerator and denominator images was approximately 2 gray-scales (from the camera tests described in Section 3.2.1). If video noise was the only noise present, then the ratio noise would be $\sqrt{2}$ times the camera noise, or 2.8 gray-scales, since the two video variances add. The noise remnant was then approximately 1.5 gray-scales, or 0.6%. Small camera misalignments may account for this modest deviation.

The noise-reducing effect of temporal and spatial averaging was investigated next. Using image cross sections the rms noise was estimated by subtracting a smoothed slice from its original, leaving a waveform with only high spatial frequency information (including both noise and high frequency image data). The standard deviation of this waveform was the quantity measured.

A chart depicting the noise reduction is shown in Figure 3.1-17. The RMS noise of the single frame ratio was smaller than would be expected from adding the numerator and denominator variances since there were correlated high spatial frequency variations in those images. The noise in the 3x3 pixel spatial averages of the convolution was reduced by the expected approximate factor of 3. The noise of the temporal average of 10 ratios was reduced the the expected factor of $\sqrt{10}$. The noise of the convolved average did not quite show the expected reduction, but this is understandable since it was at or below the digitization limit of the 8-bit frame grabbers.

3.1.5 Concluding Remarks for Calibration/Error Analysis

The accuracy and noise charactistics of DGV velocity measurements have been quantified by direct comparison with pitot probe measurements on a low–turbulence free-expansion laminar-flow air jet. DGV has been validated to an accuracy of 2%. The dominant noise source was identified to be video noise, which may be improved in the future by using low-noise full-frame deep-well video cameras.

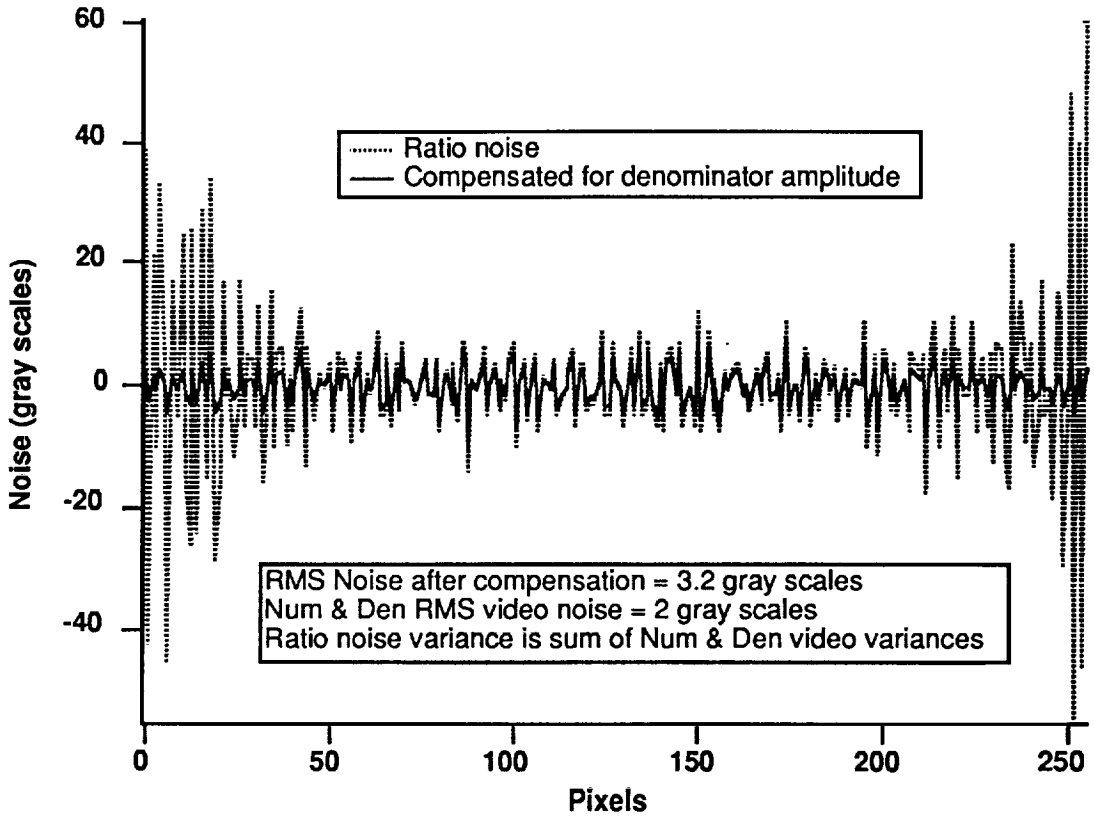

Fig. 3.1-16: Ratio image noise analysis. Denominator amplitude compensation equalizes noise cross-section ratio. Majority of noise is due to video noise.

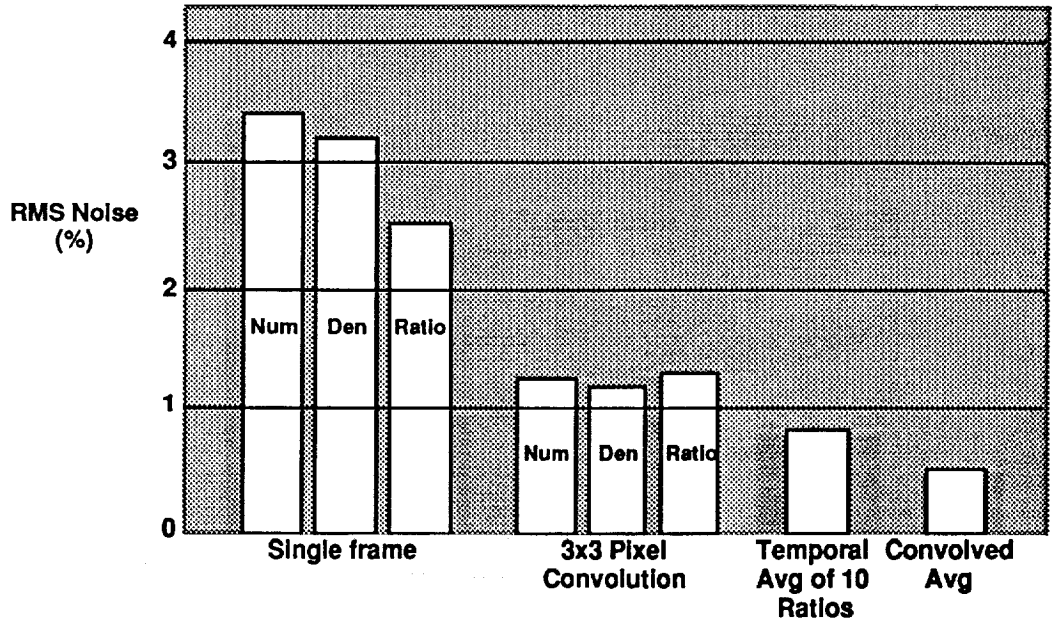

Figure 3.1-17: RMS noise comparison for single-frame images and for temporal and spatial averaging.

3.2 Component Tests and Evaluation

It is important to identify specifications of system components that critically affect DGV performance. Tests were then performed to quantify key parameters.

3.2.1 CCD Cameras Performance Evaluation

DGV performance is critically dependent upon the characteristics of the receiver CCD cameras. There is a design trade-off between camera sensitivity and laser energy. Camera noise is one factor that sets a minimum resolvable velocity . Electronic camera shutters greatly reduce the effect of ambient background light on the DGV measurement. A camera test station was therefore constructed to enable a systematic CCD characterization.

Camera full-scale sensitivity was measured as follows. A doubled Nd:YAG laser was used to generate a pulse of well known energy which was directed to a surface coated with MgO. The distribution of 532 nm light scattered from the screen was Lambertian to an excellent approximation. The laser spot was imaged onto the subject CCD sensor and was captured by a computer-based frame grabber. A physical length scale factor was measured by placing a ruler at the MgO screen and then capturing a video frame. Using this factor the pixel value was expressed as a fluence J/A (energy/area in units of J/cm^2). The energy from an area element A_{pix} that was imaged onto a single CCD pixel was related to the number of absorbed photons N_{pix} by the relation

$$N_{pix} = \frac{J}{A}\frac{A_{pix}}{h\nu}\left(\frac{D}{2L}\right)^2$$

where D is the camera aperture diameter, L is its range to the scatter screen, h is Planck's constant, and ν is the laser frequency.

Camera noise was measured as follows. A tungsten white light source was apertured and imaged onto a 1 mm diameter flat-intensity spot on the camera sensor. The image was grabbed by the computer and a cross-section was taken across the spot. A linear fit was made to the waveform and subtracted from the original to yield only a video noise waveform, whose RMS standard deviation was recorded. It is expressed in equivalent photons/pixel in Table 3.2-1 below.

Table 3.2-1: CCD Camera Measurement Results

Camera	Max Video (hν/pix)	RMS Noise (hν/pix)	Shutter
Cohu 4810	51,600	400	no
Pulnix TM-745E	234,000	1760	100 μs
Sony XC-77RR	452,000	2350	280 ns
Cohu 4910, low gain	260,000	1720	100 μs
Cohu 4910, high gain	6,900	190	100 μs

The Pulnix camera had an option that provided a flatter modulation transfer function. This feature would provide better high spatial-frequency response and more accurate DGV measurements. The small size and weight of this camera would be additional advantages for in-flight use.

The short shutter capability of the Sony camera was impressive. A pulsed laser source was used to illuminate the sensor and no synchronization problems were encountered. The camera and frame acquisition system were then taken outdoors to obtain a quantitative measurement of the solar background and of its suppression when shuttered. Some "smearing" background was observed, which is a known shuttered-CCD effect due to background light while the shutter is closed. In fact, the 100 μs shutter minimum of the other shuttered cameras (all of which use the Sony sensor) may reflect a design decision that 100 μs is the practical minimum. Therefore, even though the short shutter should in principle be able to suppress the solar background completely, some spectral filtering will still be required. Our preliminary estimate is that a 10 nm interference filter should be adequate.

The Cohu 4910 had an adjustable gain control which was active when the AGC was disabled. The sensitivity and noise data for both cases is shown in the table. For the high gain case, the video noise is noticeable (≈ 3%). Temporal or spatial averaging would of course be available if needed.

The results of the receiver signal to noise analysis (Section 3.4.5) indicate that for conditions of high solar background ($\approx 10^6$ photons/pixel) a gated camera with deep pixels ($\approx 10^6$ electrons) is required to attain a velocity accuracy of 1 m/s. The Sony camera comes closest to this specification, while bringing the added advantages of a potentially narrower gate time interval and small size. Of the cameras surveyed, it alone can meet the 1m/s accuracy specification.

3.2.2 Iodine Cell Fabrication Methods and Tests

The optical quality of the ALF cell is an important DGV receiver specification. Cell window distortions can make pixel overlap of ALF and reference images impossible without difficult and potentially inaccurate image processing to "dewarp" the distorted image. We have acquired cells whose windows were attached by both fusing and optical contacting techniques and have performed interferometric measurements of their optical distortions. Cells with fused windows showed significant distortions (Figure 3.2-1). Cells with optical contacted windows showed virtually no distortion and should be the design specification.

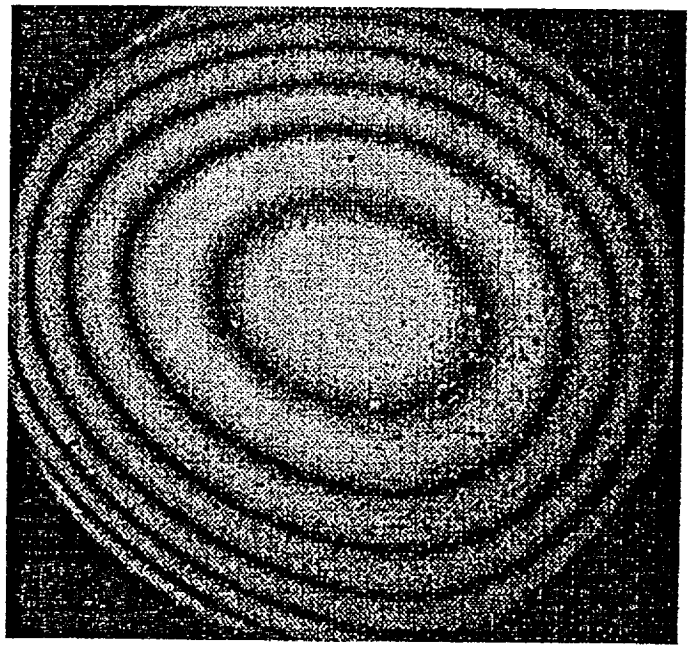

Fig 3.2-1: Interferogram of ALF cell with fused windows. Note the oblong fringes indicating distortions in addition to optical power.

3.2.3 Optical components

The polarization of light scattered from particles seeded into the flow is a sensitive function of scattering angle. The polarization dependence of the receiver's tilted beamsplitter should be minimized and is an important receiver specification since it results in a velocity measurement offset error. The receiver optics and cameras were laid out to minimize the beamsplitter angle, to maximize camera field-of-view, and to allow the adjustments defined in Section 3.1.2. The resulting beamsplitter angle was approximately 20°.

The angular dependence of the reflectance versus polarization for the beamsplitter used in the current DGV receiver is shown in Figure 3.2-2. There is approximately a 9% transmission difference between the two polarizations for a 20° angle of incidence, corresponding to a velocity offset of approximately 20 m/s. Such an offset could be found by comparing the measured transmission of the frequency control reference cell with the transmission measured from the video ratio. Any deviation could be compensated for with a small ALF cell temperature change. Such adjustment would only be required when the location of the camera or the lightsheet orientation is changed.

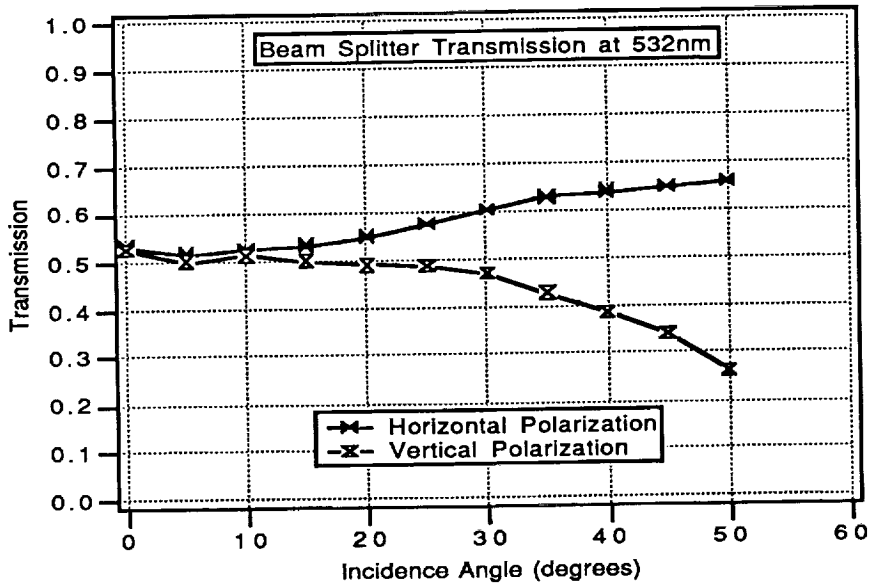

Figure 3.2-2: Transmission of beamsplitter versus angle of incidence for horizontal and vertical polarization.

3.3 Laser/ALF Study

This section presents the results of a trade-off study on lasers and ALF media for a flight measurement DGV system. The study included:

- ALF surveys on atomic and molecular media
- Matching tunable lasers
- Laser technology assessment and ranking
- Flight System DGV Laser/ALF Considerations

DGV systems for installation on an airplane or in a wind tunnel will require further development of lasers that are compatible with the platform/environmental characteristics. The choice of a laser system for flight measurement is primarily dictated by size and weight requirements; however, the laser wavelength must also match the ALF lines. Thus, we first surveyed the ALF candidates, and then considered various lasers with matching wavelengths. Next, we made an assessment of technology status for these lasers and ranked them according to relative probability of success.

As a result of these surveys and assessment, we selected iodine ALF and frequency-doubled, Nd:YAG/YLF/YAP lasers as the prime candidates for further engineering development at this time. This selection will permit two different DGV configurations for the flight measurement system on a platform such as the F-18 HARV. The following sections present the details of our study, and we conclude with a recommendations for future work.

3.3.1 ALF Media Survey

Absorption line filters utilize very narrow transition lines in atomic and molecular vapor cells. Transitions in the visible and near-infrared bands are considered in this survey since CCD detectors used in the DGV receivers have spectral response over that region.

The following sections describe some of the molecular and atomic vapors that have absorption lines in the desired spectral regions. The survey concludes with a recommendation for an ALF candidate.

Molecular Vapor— Although a wide variety of molecular gases and vapors exhibits visible and near-infrared absorption bands, only a few can meet the ALF requirements. These requirements include isolated, strong transition lines with low background absorption and a smooth spectral profile. These criteria narrow the choices to low pressure, diatomic molecular vapors with distinct absorption spectra.

Molecular iodine and bromine are two candidates that have well known absorption lines in the visible region (500-600 nm for iodine, 530-570 nm for bromine). Alkali and other dimers (e.g., sulphur, tellurium, etc.) also have distinct absorption lines, but they require relatively high temperatures (several hundred degrees C) to yield adequate vapor pressures.

Both iodine and bromine vapor pressures are easily controlled by temperature near room temperature. For a 5 cm long iodine cell, near extinction at line center can be achieved at a temperature of about 40 C. The cell transmission is greater than 90% at frequencies detuned far from the line center. In contrast, bromine vapor absorption lines show a substantial amount of broadband absorption which reduces the dynamic range of cell transmission. Therefore, molecular iodine is the best candidate in the molecular vapor category.

Atomic Vapor— Alkali atoms provide a number of isolated transitions as listed in Table 3.3.1. These so-called resonance lines are useful as narrowband filters as well as absolute frequency reference for laser radiation. Each line consists of underlying hyperfine transitions which are normally unresolved due to Doppler broadening.

Table 3.3.1 Atomic Vapor ALF Candidates

Atomic Vapor	Transition Wavelength (nm)
Cesium	455.54 459.32 852.11 894.35
Rubidium	420.19 421.56 780.02 794.76
Potassium	404.41 404.72 764.49 769.90
Sodium	588.99 589.59

The sodium D-lines are well known in laser spectroscopy due to a spectral match to dye lasers. Recently, cesium and rubidium resonance lines have been used to stabilize the frequency of laser diode output that matches the transition wavelengths. Detailed spectroscopic data on these transitions indicate that alkali atoms can meet the ALF requirements. Cesium and rubidium are especially attractive since extinction at line center can be obtained at moderate temperatures (50-100 C).

Recommendation for ALF Development— The ALF media survey indicated that molecular iodine and atomic cesium/rubidium are clear choices for DGV applications. Our DGV work has already demonstrated molecular iodine as an ALF medium; however, a cesium or rubidium ALF has yet to be tested. Since cesium/rubidium cells can be fabricated using methods similar to those used for molecular iodine cells, an alkali vapor ALF could be developed in a straightforward way.

3.3.2 Matching Tunable Lasers

The requisite characteristics for a DGV laser include emission wavelength, bandwidth, pulse length, pulse energy, and pulse repetition rate. Table 3.3.2 shows a list of lasers with output wavelengths and the matching ALF media.

Table 3.3.2 Matching Tunable Lasers and ALF Media

Laser	Wavelength (nm)	ALF Media
Nd:YAG/SHG	532	I_2
Nd:YLF/SHG	523.5, 526.5	I_2
Nd:YAP/SHG	539.5	I_2
Ti:Sapphire	650-1000	Cs, Rb
Alexandrite	730-780	Rb
Pulsed Diode	830-980	Cs

3.3.3 Laser Technology Assessment for DGV

Evaluation criteria for laser technology assessment include R&D status, commercial availability, reliability, and suitability for DGV. Development trade-offs and probability of success are derived from this assessment. The current status of the matching lasers is summarized below in ranking order.

Solid-State Lasers — The neodymium lasers with different host materials emit at slightly different wavelengths near 1 micron. Frequency-doubling of these lasers generates the green wavelengths that match the iodine transitions. These lasers can be tuned over a frequency range of more than 30 GHz (1 wavenumber). Figure 3.3.2-1 shows detailed iodine absorption spectra near the green laser wavelengths. Several transitions are accessible for each of the candidate lasers.

The operating characteristics of these Nd:host lasers are similar, but Nd:YAG is the most developed device. Commercially available, pulsed Nd:YAG lasers with single-frequency output and tuning control can be readily integrated into a DGV laser system. Other Nd:host lasers can be custom built for DGV; however, single-frequency operation requires seed lasers that have been demonstrated only in the laboratory.

A Nd:YAG laser has also been developed for a military flight system by McDonnell Douglas Electronic Systems Co.[7] This laser is used in a rangefinder that was test flown on F/A-18 fighter aircraft starting in 1990. Air-cooled diode arrays pump this laser which emits 1.064 μm or 0.532 μm at a pulse width of 9 to 30 nsec and an output energy per pulse of up to 200 mJ. The laser requires 200 W when firing at 20 pulses per second. The operating temperature range is from -35 to +65 C. The unit occupies only 200 to 400 cubic inches and weighs 10 to 15 lb.

The titanium doped sapphire laser is a tunable solid-state laser with relatively efficient output between 700 nm and 900 nm. This laser is usually pumped by another laser (e.g., frequency-doubled Nd:YAG or argon ion laser). Commercial devices with single-frequency output and tuning are available. Such a Ti-sapphire laser is a DGV laser candidate when it is matched with cesium and rubidium ALF. However, one major disadvantage of this laser is its relative complexity and the added cost of the pump laser.

Chromium-doped crystals represent another class of lasers with a limited tuning range in the 700 nm to 1000 nm region. Alexandrite, LiCAF, and LiSAF are recently developed host crystals that can be flashlamp pumped to produce Joule-level output pulses. These lasers are at a relatively early stage of commercial development; they are not DGV laser candidates at this time but may be useful if high pulse energies become necessary in certain conditions.

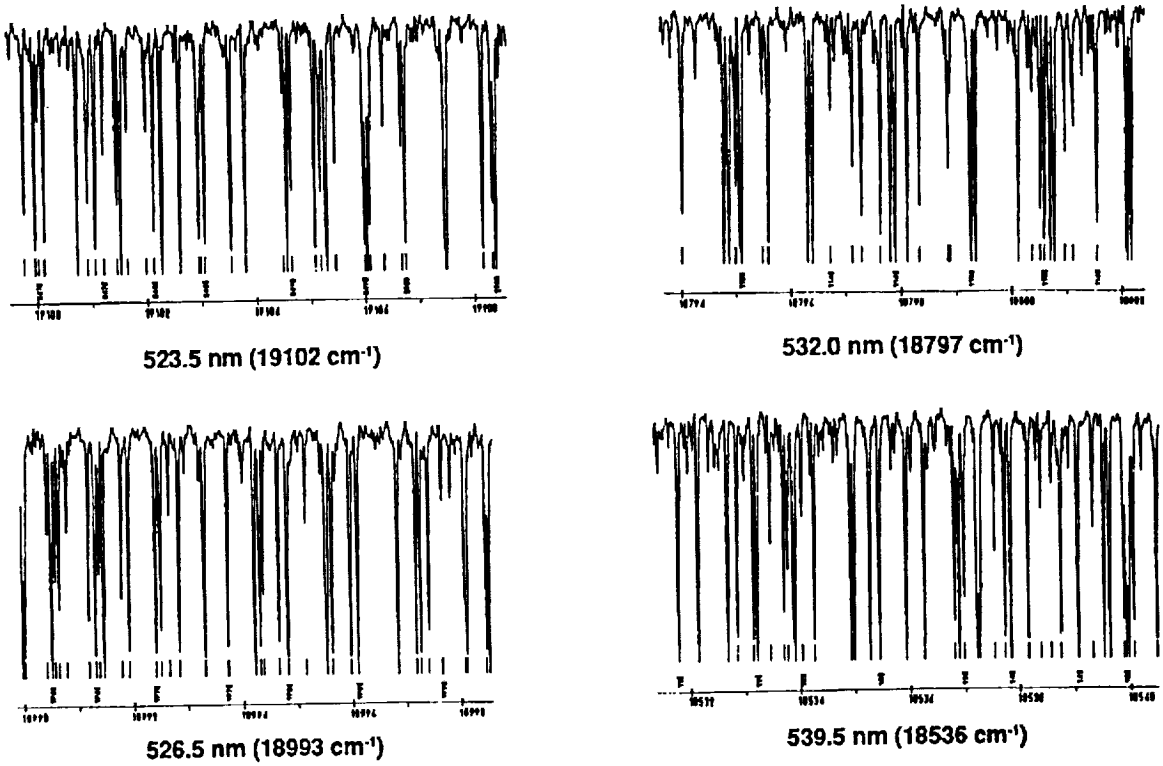

Figure 3.3.2-1: Relevant regions of iodine absorption spectra for frequency doubled Nd:Host lasers. Source: Spectre Moleculaire de L'Iode Lab. Aime Cotton Orsay-France[8].

Semiconductor Lasers— Semiconductor laser diodes have made significant advances in output power, efficiency, and reliability over the past several years. These lasers are attractive for DGV because of their compact size. However, diode laser spectral characteristics pose challenging problems for DGV use at this time.

Single-frequency, continuous-wave (CW) diode lasers are commercially available with single-stripe geometries. These devices emit at relatively low power levels (i.e., less than 1 W). Commercially available high-power devices (10-15 W) use an array of diodes with a spectral distribution of about 2 to 3 nm. Various methods have been tried to lock the lasing frequencies of these diodes to a single frequency, but these techniques are still at experimental stages. Currently, only the single-stripe diodes appear to be readily useful as an injection seed source for Ti-sapphire lasers. For the DGV application, the diode power supply current and diode temperature must be controlled precisely to maintain a stable output frequency. Stringent stabilization is required to adequately maintain the laser frequency to DGV specifications. Such devices are not yet commercially available.

In contrast to CW diode lasers, pulsed diodes emit chirped output spectra that result in bandwidths of about 3 to 4 nm. This is not suitable for DGV. Joule-level Nd:YAG lasers have been built with diode arrays; however, such systems are still considerably more expensive than flashlamp-pumped lasers with the same output energy. Ultimately, diode-array-pumped solid-state lasers are the most attractive devices for DGV, especially for flight measurement applications.

3.3.4 DGV Flight System Laser/ALF Considerations

The results of the ALF survey and laser technology assessment show that the best candidates enable us to consider two DGV configurations. The first configuration uses one laser to generate the light sheet and three identical receivers with the same ALF. This case, denoted as "R3" configuration, is based on the simultaneous three-component DGV concept developed at Northrop[2]. The second configuration, suggested by NASA for flight systems, uses three different lasers ("L3") each generating one light sheet and three co-axially aligned receivers. Three receivers with different ALF media are used when simultaneous three-component measurements are required.

The R3 configuration requires a frequency-doubled Nd:YAG laser and molecular iodine ALF for the three receivers. Since these elements have been successfully tested under the calibration and error analysis task, the R3 approach is founded on demonstrated capabilities.

The main advantage of the L3 configuration is the common optical axis of the three receivers. Such an arrangement simplifies image overlap and reduces perspective-induced errors; however, the L3 configuration does have drawbacks as well. For example, the three different laser light-sheets must be coplanar to within the sheet thickness.

Assuming that the coplanar laser light-sheets can be achieved, we now consider how the receivers can distinguish the matched laser wavelength. In principle, a narrow bandpass optical filter can block all wavelengths except the matched laser wavelength. In the case of three Nd:host lasers, the green wavelengths can be individually isolated by interference filters with a bandwidth of about 3 nm. The individual laser frequency is tuned to match a suitable iodine absorption line within that filter transmission window. A similar strategy applies for a laser system based on three Ti-sapphire lasers and three cesium/rubidium ALF units. Thus, the L3 configuration can be implemented, in principle, using the candidate lasers and ALF media.

However, the benefits of the L3 image alignment must be weighed in view of the added complexity of three different laser systems and ALF media. From a reliability standpoint, the increased system complexity carries a higher probability of single point failures. The L3 system cost is anticipated to be considerably higher than that of the R3 system, mainly due to the cost of two additional lasers.

In conclusion, our recommendations for the lasers and ALF media allow two DGV configurations for flight measurement systems. Diode-pumped solid-state lasers will be a key part of these systems.

3.4 Flight Measurement System Outline

The Doppler global velocimeter offers a unique opportunity to apply a new diagnostic tool for flow field measurements in flight. In contrast to previously developed velocimeters, DGV has the potential for acquiring three-component velocity data in near real-time during flight maneuvers. This capability, if realized, would represent a major advance in flight testing.

In particular, a flight DGV system for NASA's High Angle-of-attack Research Vehicle (HARV) program was considered as a goal for this work. Figure 3.4.0-1 illustrates the proposed locations of measurement planes between stations 440 and 524. A preliminary goal is to obtain three-component velocity data for vortical flow fields over a 2 meter by 2 meter region above the wing. The desired measurement accuracy is 7% with a spatial resolution of 1 cm. The measurements would be carried out at angle-of-attack values of up to 50 degrees.

The base period of this work addressed the feasibility of such a system by identifying the essential characteristics of a flight measurement system for the HARV. The result is an outline that establishes a preliminary basis for system configurations. We analyzed measurement errors, installation issues, and operating requirements for these configurations.

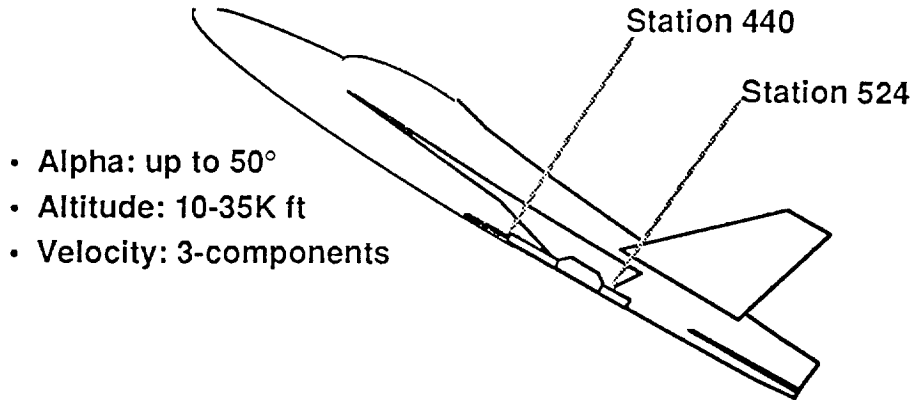

Figure 3.4.0-1 Test Conditions for F-18 HARV DGV Experiment

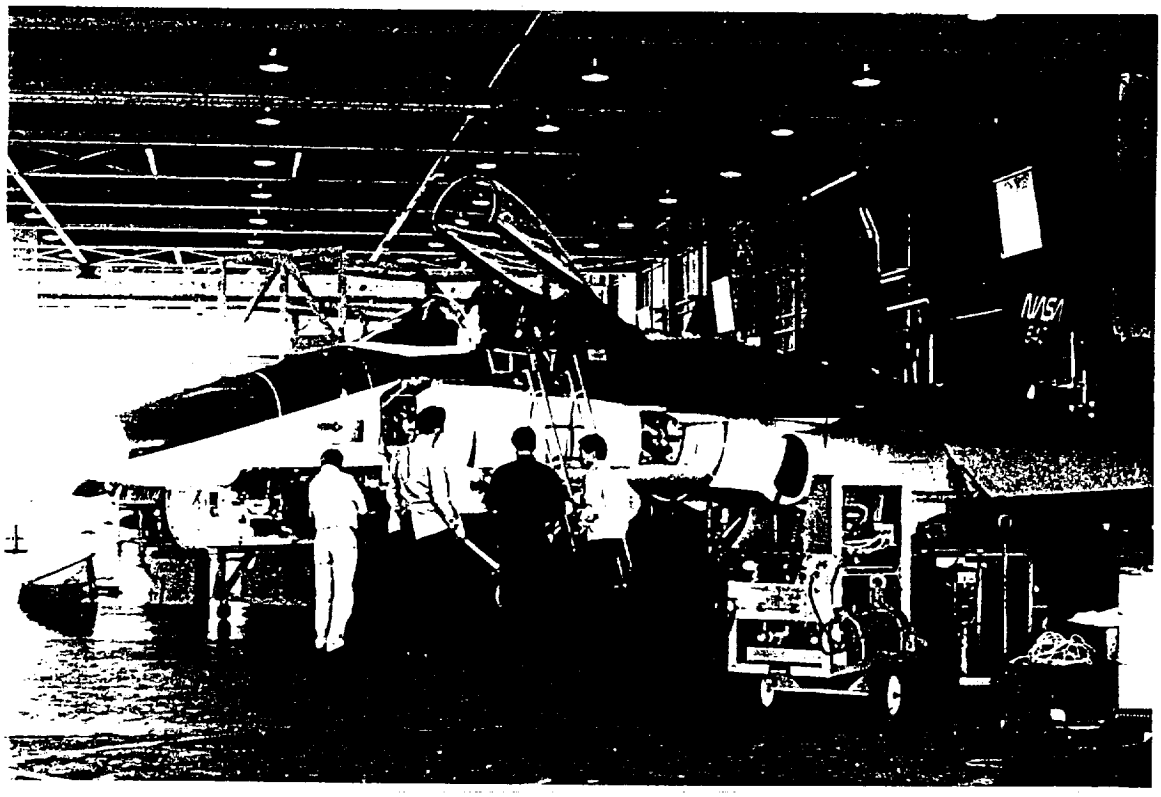

Figure 3.4.1-1: F-18 HARV inspection at NASA Dryden facility

3.4.1 F-18 HARV Inspection at Dryden

We visited the NASA Ames/Dryden Flight Test Facility in order to inspect the F-18 HARV aircraft, as shown in Figure 3.4.1-1. Cooperation from the engineering/technical staff on the HARV aircraft enabled us to obtain valuable information about the plane and its existing instrumentation. A video tape summary of the HARV flight tests was especially helpful in understanding the aircraft behavior under test conditions. As a result of these discussions and inputs, we formulated two design configurations for a DGV system on the HARV aircraft. Figure 3.4.1-2 shows schematics of these configurations.

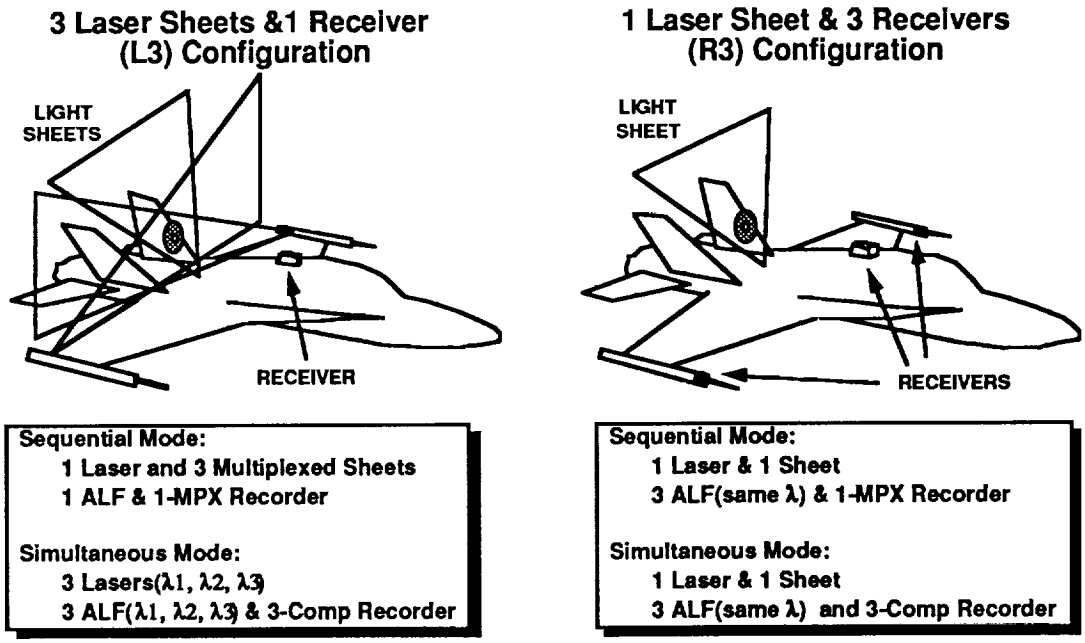

Figure 3.4.1-2 DGV Flight System Configurations

We considered sequential and simultaneous modes of measurement for acquiring three velocity components. The sequential mode is conceptually simpler to develop; however, a disadvantage of this mode is that velocity components are not temporally correlated. The simultaneous mode permits temporally correlated measurements, but the system requires more complex hardware, especially for the (L3) configuration that uses three lasers.

3.4.2 DGV Configurations for HARV

The two DGV configurations proposed for the F-18 HARV platform measure the velocity components along different directions. Although these components are transformed into a coordinate system suitable for the platform, measurement errors are not the same in the two cases. This section presents an analysis of velocity measurement errors that result from geometrical effects. We will also address optical alignment requirements for simultaneous three-component measurements.

Geometrical Measurement Errors— In the three-laser (L3) configuration being considered for the flight system, three light sheets are generated: one from each wing tip and a third sheet from a point on the fuselage. A receiver system is assumed to be mounted in the turtleback on the fuselage behind the cockpit. We have analyzed velocity measurement errors for this geometry using a computer model. The model includes the effect of angular spread of light sheet and observer direction for each point in the measurement plane. It is found that errors become relatively large in certain regions of the measurement plane. As explained below, this effect is caused by the geometry of laser and observer vectors for which 3-component calculation becomes nearly indeterminate. In general, regions well above the wings showed a minimum amount of errors; a narrow sector just above the wings indicated the greatest errors.

Figure 3.4.2-1 shows a coordinate system used for the F-18 HARV platform in carrying out the model calculations for the L3 configuration. The wind direction is defined as the x-axis. The y and z axes are defined along the wing and azimuth directions, respectively. Light-sheet illumination is assumed to be parallel to the yz-plane

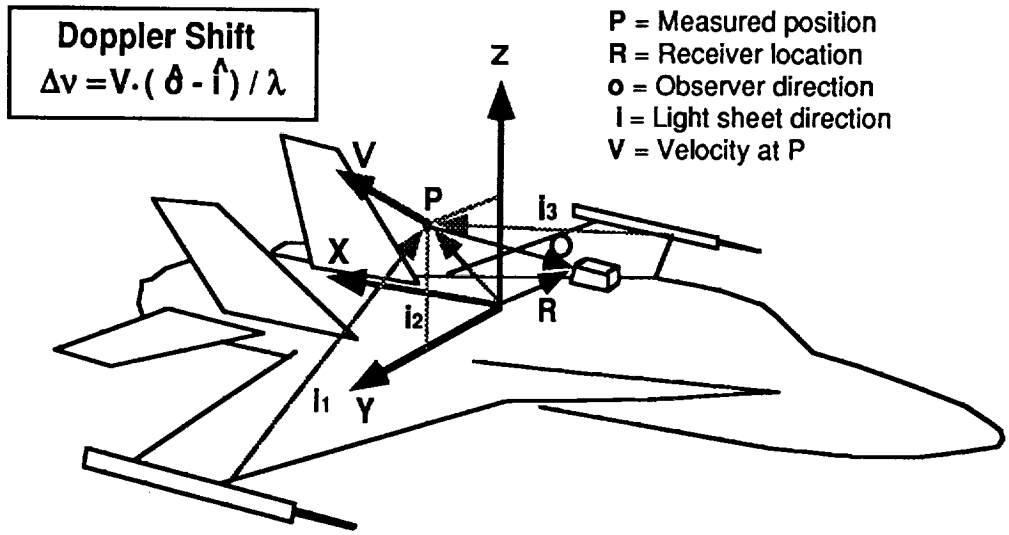

Figure 3.4.2-1: Coordinate system for F-18 HARV

In the three-receiver (R3) configuration (see Fig. 3.4.1-2), each receiver observes one common light-sheet which is located on the fuselage. Two of the receivers are placed on the leading or trailing edge of each wing-tip rail-pod, and the third one is located at the same turtleback position as in the L3 configuration. We have also analyzed velocity measurement errors for this geometry and found results which are similar to those of the L3 configuration.

The DGV system measures three components (not necessarily perpendicular) of the air velocity at each point in a plane. The direction of these components depends on the relationship between the point in the measurement plane (light sheet) and the source and observation points. Any error in the determination of these components becomes an error in the inferred Cartesian components of the velocity. Uncertainty may also arise due to errors in measuring intensity (electronic or background noise) or errors in translating frequency shifts into intensity (ALF response, frequency jitter).

The three measured velocity components are given by

$$u_n = (\mathbf{o}-\mathbf{i}_n)\cdot\mathbf{V} \quad \text{(L3 case)} \quad \text{or} \quad u_n = (\mathbf{o}_n-\mathbf{i})\cdot\mathbf{V} \quad \text{(R3 case)}$$

where n=1,2,3 denotes three lasers or receivers. **o** is the unit vector from the measurement point to the receiver, and **i** is the unit vector from the laser to the measurement point. The first equation assumes three lasers and one receiver, and the second equation assumes one laser and three receivers. In either case, the equation can be solved for **V** by matrix inversion as

$$\mathbf{V} = \sum_n (\mathbf{o}-\mathbf{i}_n)^{-1} u_n$$

Thus each Cartesian component of **V** is just a weighted sum over the three measured components, u_n. If the error in u_n has a Gaussian distribution, then the error in **V** is given by

$$\Delta\mathbf{V} = \left[\sum_n \left|(\mathbf{o}-\mathbf{i}_n)^{-1}\right|^2 \Delta u_n^2\right]^{\frac{1}{2}}$$

where $\Delta\mathbf{V}$ represents the standard deviation.

The error field is plotted in Figures 3.4.2-2 as the ratio of $\Delta\mathbf{V}$ to Δu_n, assuming $\Delta u_1=\Delta u_2=\Delta u_3$. Figure 3.4.2-2(a) is for three lasers/one receiver (L3) and Figure 3.4.2-2(b) is for three receiver/one laser (R3). The error ratio is between one to two for most of the x-component (direction along relative wind) and y-component (direction along wing plane, orthogonal to relative wind) except near the bottom of the field-of-view (FOV). (FOV in this calculation is a 2m by 2m square with the lower left corner on top center of the fuselage, 3m aft of the fuselage receiver). The z-component (orthogonal to relative wind and wing plane) has errors of 2 to 5 times the measurement error near the top of the FOV. Along the line of maximum uncertainty, the three vectors $\mathbf{o}-\mathbf{i}_n$ or $\mathbf{o}_n-\mathbf{i}$ all lie nearly in a plane. Since this plane is nearly parallel to the x-y plane, the z-component has the greatest error.

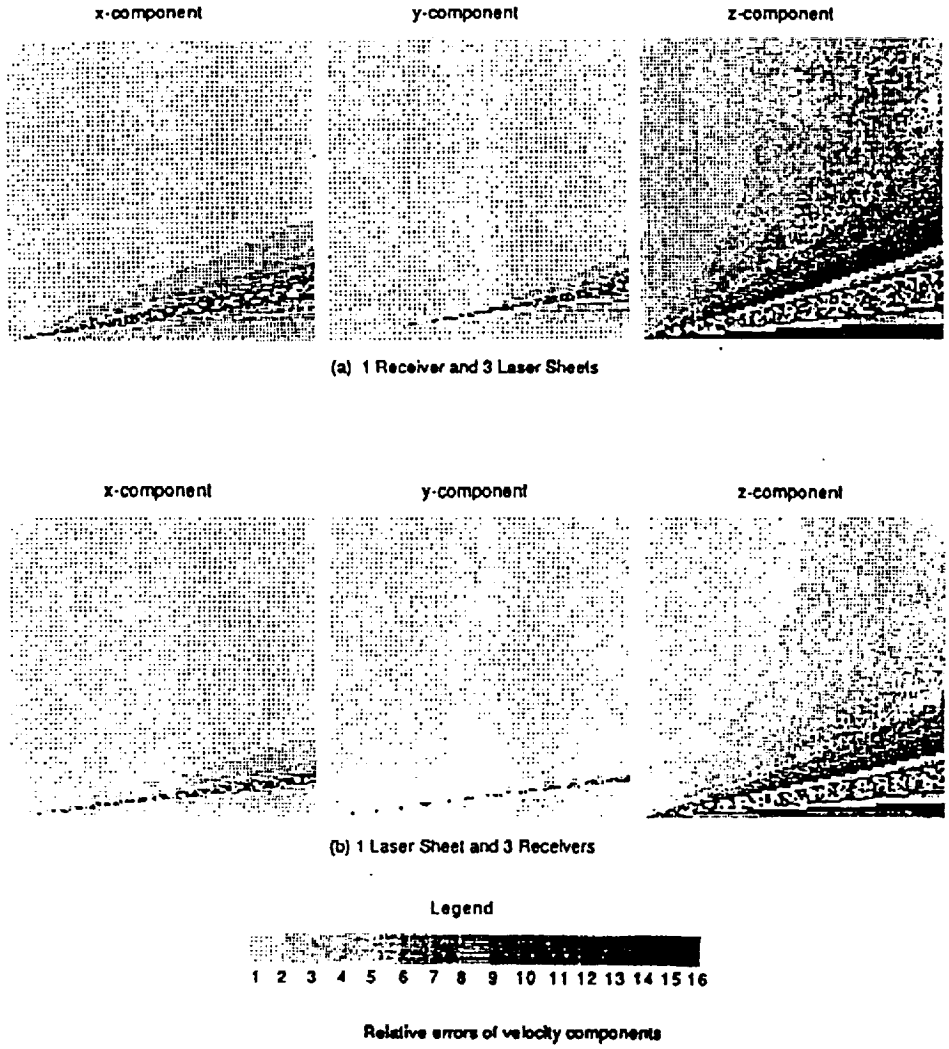

Figure 3.4-2: Calculated error field for (a) L3 and (b) R3 configurations. Dimensions are 2mx2m. Lower left corner is at the receiver in the F-18 turtleback.

The errors described above are relative to the errors picked up by the camera/filter system. To keep the maximum error in determining each velocity component to less than 7%, the individual measurement errors must be less than or on the order of 2%. Additional errors arise from uncertainties in the vectors **o** and **i** since the relative positions of receiver and laser may change with time. Also errors due to a finite number of pixels per resolution cell may occur, especially for cameras viewing the light-sheet from the side. Overlapping or misalignment of pixels may affect resolution as well as accuracy.

Optical Alignment Requirements— The model calculations assumed that light sheets are coplanar in the L3 case and that receiver directions are stationary for the R3 case. If these assumptions are not satisfied measurement errors are introduced into the three-component calculations.

The spatial resolution requirement is 1 cm in all dimensions. This means that velocity vector components must be measured and spatially correlated to within that volume element. In the L3 case, light-sheets must intersect each other in a common plane with displacement errors of less than 1 cm along the x axis. The corresponding angular tolerance is about 2 milliradians about the y and z axes. Therefore, the three light-sheets are required to maintain plus or minus 1 milliradian of angular deviation from the coplanar condition.

The angular deviation must be monitored for each data set. Satisfactory overlap of the light-sheets is a necessary condition in order to compute spatially correlated velocity components. Otherwise, the data set cannot be processed to yield a valid velocity vector field with the required spatial resolution.

In the R3 case, a single light-sheet can define a very thin (≈1mm) measurement plane since overlapping sheets are not required. This removes the stringent angular tolerance on the light-sheet and lessens the such complications as perspective corrections, which can be accommodated in software. However, each of the three receivers must be oriented to allow image overlap to within the spatial resolution requirement. This means that the relative position of the receivers must be known for each set of images.

A position monitor for each receiver must be built into the platform to satisfy the image registration requirement. An auxiliary camera mounted with each receiver can record such displacements using fiducial markers that are fixed on the airframe. Unlike the three laser light-sheet case, each image data set obtained with the displacement data can be processed with the required spatial resolution using software to correct any image registration errors.

In summary, the optical alignment requirement is different in the two DGV configurations. Each configuration demands a monitor data to correct for displacement errors. The L3 configuration must ensure overlapping light-sheets with hardware compensation; otherwise the data is not correlated. The R3 case permits software corrections as part of image processing algorithms, which provides an added flexibility in data recovery.

3.4.3 Mounting Considerations

The possible locations of laser light-sheet and receivers on the F-18 HARV airframe are practically limited to existing instrumentation pods on the missile rails and a turtleback behind the cockpit. Discussions with the HARV technical staff indicated that another turtleback on the fuselage may be possible without affecting air flow over the wings.

Turtleback— This area currently houses a camera as shown in Figure 3.4.3-1. Figure 3.4.3-2 shows the available space underneath the turtleback, which measures about 4" x 16" x 25". The temperature in this area becomes very warm during flight. Thus, any electronic instruments (including lasers and receivers) installed in this space must be thermally isolated and cooled. Power access is available through a bulkhead at the rear of the cockpit; however, this area is heavily used to route various cables.

Rail Pods— A missile rail on each wing tip can carry instruments with dimensions of up to about 8" x 8" x 12". Currently the pods house a video camera and other probes. Figure 3.4.3-3 shows one of the instrument pods. According to a HARV engineer, the length and the shape of this pod can be modified. Air cooling may be possible for instruments in this pod. Thus, the pods provide a working environment to house a laser or DGV receiver.

A primary concern for mounting lasers and receivers in the pods is the relative displacement of wing tips during flight. We obtained wing tip deflection data for an F-18 aircraft under various flight conditions. The definitions of those conditions are described in Table 3.4.3-1.

Table 3.4.3-1 Critical Design Conditions for F/A-18 Wing

Cond.	Weight (lb)	Altitude (ft)	NZ (G's)	Mach No.	C.G. (%)	Description
W034L	31000	20000	6.0	1.1	23.5	Wing bending with down aileron
W034R	31000	20000	6.0	1.1	23.5	Wing bending with up aileron
W035	31000	Sea Lev	7.5	0.85	19.1	Symmetrical pull-up Max. leading-edge-flap loading
W037	31000	15000	7.5	1.0	19.1	Symmetrical pull-up Max. wing root bending
W038	31000	Sea Lev	7.5	0.55	23.5	Wing bending with high leading/trailing-edge-flap deflections
W039	31000	35000	7.5	1.2	19.1	Wing bending with high trailing-edge-flap loading
W040	37894	10000	2.0	0.54	19.6	Landing approach with high wing loads
W042R	31000	20000	1.0	0.95	23.5	Max. hinge moment for up trailing-edge flap

Figure 3.4.3-1: F-18 HARV with fuselage top cover removed aft of camera turtleback.

Figure 3.4.3-2: F-18 HARV space underneath turtleback

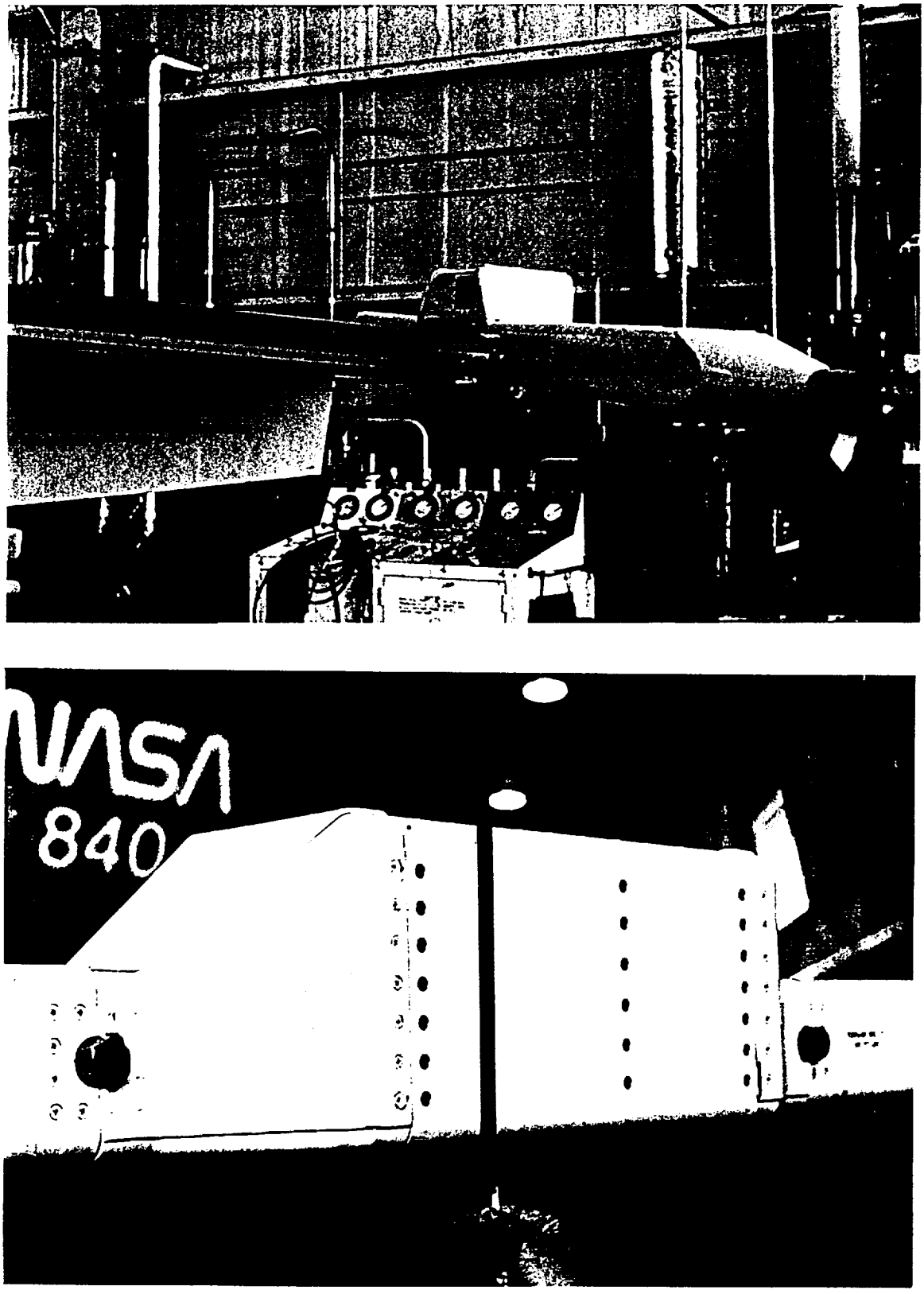

Figure 3.4.3-3: HARV instrument pod on wingtip rail. Top: front view. Bottom: side view, close up.

Table 3.4.3-2 lists the coordinates of three test positions along the missile rail. Table 3.4.3-3 shows the deflections at those positions under the defined flight conditions (Table 3.4.3-1).

Table 3.4.3-2 F/A-18 Wing Tip Outboard Edge Point Locations

Position	Fuselage Station F.S. (inch)	Butt Line B.L. (inch)	Water Line W.L. (inch)
Point A	506.769	225.253	102.039
Point B	515.261	225.291	102.781
Point C	525.291	225.326	103.432

Table 3.4.3-3 F/A-18 Wing Tip Limit Deflections (inch.)

Condition	Point	B.L.	F.S.	W.L.
W034L	A	.6043	-.2347	13.2735
	B	.5491	-.2660	13.6519
	C	.5086	-.2936	14.0904
W034R	A	.4072	-.0362	9.3093
	B	.3415	-.0228	9.1637
	C	.2831	-.0010	8.9860
W035	A	.7748	-.2212	17.2698
	B	.6733	-.2215	17.2851
	C	.5894	-.2216	17.2967
W037	A	.8227	-.3329	18.0717
	B	.7354	-.3575	18.3711
	C	.6694	-.3773	18.7018
W038	A	.7481	-.4810	15.6885
	B	.6881	-.5118	16.0626
	C	.6471	-.5385	16.4925
W039	A	.7858	-.3579	17.1109
	B	.7169	-.3994	17.6087
	C	.6680	-.4357	18.1849
W040	A	.4154	-.1141	9.3803
	B	.3788	-.1445	9.7407
	C	.3529	-.1708	10.1576
W042R	A	-.0378	.1880	-.0096
	B	-.0653	.2120	-.2968
	C	-.0935	.2344	-.6388

Positive deflections move wing tip points outboard (B.L.), upward (W.L.), and backward (F.S.).

Clearly, severe wing warping occurs at high-G maneuvers; however, flight test conditions envisioned for the HARV experiment (as represented by the bottom row W042R in the table) lead to displacements of less than a few centimeters. In particular, positions A and B show

deflections of less than 1 cm. This suggests that a proper placement of lasers and receivers along the rail should be considered for installation.

Light-sheet- The top of the fuselage is a possible location for laser light-sheets. We studied various methods of beam delivery from the laser to the origin of the light-sheet fan.

Optical fibers provide a convenient way to route beams; however, several trade-off issues became evident when we considered the laser pulse energy and peak power requirements. First, multimode fibers are needed to transport 100 mJ pulses with 10 nsec duration. Such fibers have a minimum bending radius of about 30 cm, which creates routing difficulties inside the wing and fuselage. Second, multimode fibers degrade the spatial coherence of the laser beam. Thus, light-sheet thickness cannot be maintained at 1 cm or less over the measurement plane.

An alternative approach uses free-space beam routing above the wing. In this case, a laser beam is first directed at relay optics on the fuselage. The relay optics contain lenses and mirrors to form a light-sheet fan and to direct it to the measurement plane. An active beam positioning mechanism may be used to maintain the link alignment between the laser and the relay optics. This approach also has an advantage of higher power handling capabilities compared with that of the optical fibers. Therefore, we recommend the free-space beam routing for the HARV platform.

3.4.4 Smoke Seeding Requirements

The flight system under consideration assumes the use of existing smoke generators on the F–18 HARV. An estimate of seed particle density produced by the on-board smoke generators indicates that there will be an adequate amount to scatter the laser light.

An estimate of the particle density can be made as follows. The number of particles generated by the smoke bomb during its burn time is equal to the number of particles in a cylinder with a cross section equal to the smoke column area at the light sheet location, and a length equal to the distance traveled by the aircraft during the burn time, i.e.:

$$\frac{V_b}{V_p} = nvAt_b$$

or

$$n = \frac{V_b}{V_p vAt_b}$$

where:

V_b = smoke bomb volume = 10^3 cm^3
t_b = smoke bomb burn time = 30 sec
V_p = particle volume = 4.2×10^{-12} cm^3 (approx. average particle diameter of 2 μm)
A = area of seeded region at light sheet location = 10^4 cm^2

v = aircraft speed = 10^4 cm/sec
n = particle density (cm^{-3})

Substitution in the above expression yields n= 8 x 10^4 cm^{-3} (a more exact calculation could be made using the measured particle size distribution function). This density is about an order of magnitude larger than the one calculated from measurement accuracy considerations (see Section 3.4.5, Scatterer Density Requirement). This estimate should be confirmed by actual density measurements, but it indicates that the seed density will likely not be a significant problem for laser energies on the order of 0.1 J/pulse.

3.4.5 Receiver S/N Analysis

System analysis and model calculations addressed the effect of receiver signal-to-noise ratios on measurement accuracy. The analysis included background light and noise due to laser and receiver response. Representative conditions were used to estimate the rms error of velocity measurements due to these noise sources. We also estimated a minimum particle density which yields the assumed test conditions.

Background Light— The solar background spectral power density, $N(\lambda)$, is about $0.01 W/cm^2/\mu m/steradian$. The number of photons per pixel (n_B) on the receiver detector array due to this background is given by:

$$n_B = N(\lambda) A_r \Omega_r \Delta\lambda_r t_{int} / h\nu P^2$$

Table 3.4.5-1 lists the definition and example values for each of the parameters.

Table 3.4.5-1 Parameters for Solar Background Light Calculation

Parameters	Definition	Example
n_B	Background photons/pixel	1.8×10^6
A_r	Receiver aperture	19.6 cm^2
Ω_r	Receiver field-of-view	0.1 steradian
$\Delta\lambda_r$	Filter bandwidth	3 nm
t_{int}	Detector integration time	10^{-4} sec
$h\nu$	Photon energy	3.7×10^{-19} J
P^2	Number of pixels	9×10^3

The solar background level varies by several orders of magnitude after sunset as shown in Figure 3.4.5-1. The reduced brightness of the twilight sky can be advantageous for background noise suppression if flight tests can be carried out after sunset. The moon is not a concern since its brightness is a factor of about 10^5 less than the solar sky background.

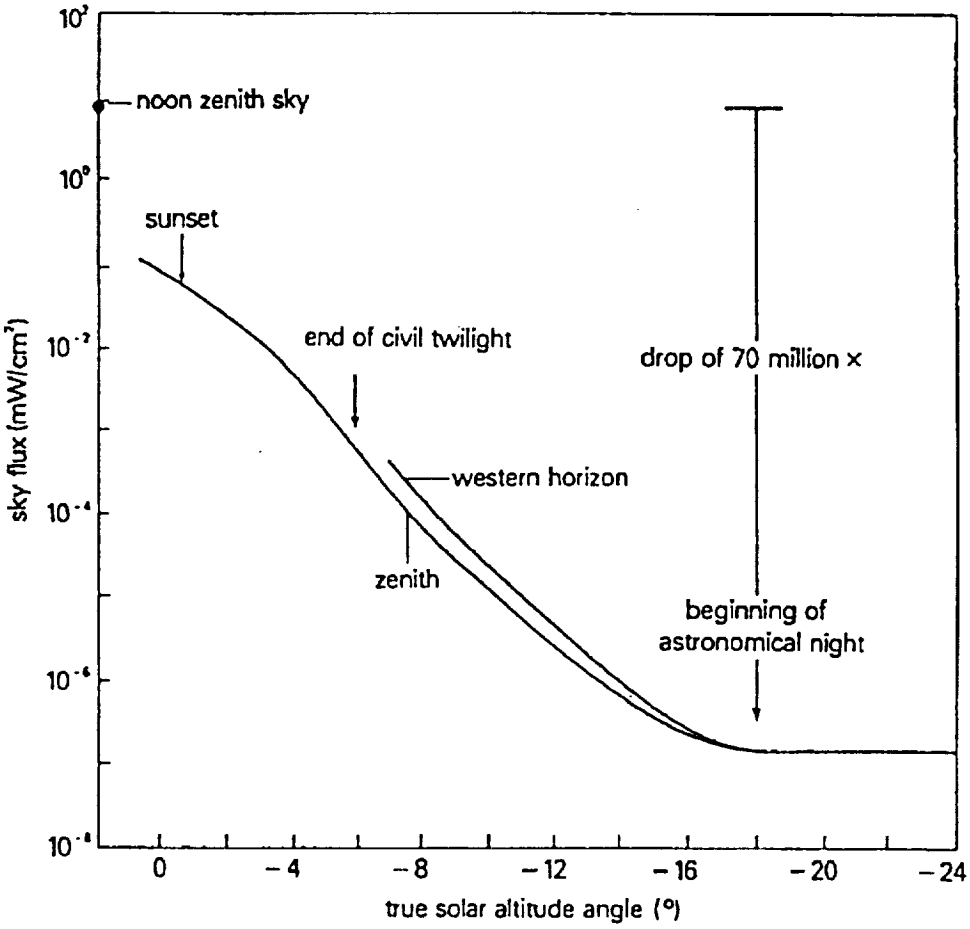

Figure 3.4.5-1: Decrease of twilight-sky brightness after sunset

Velocity Measurement Precision vs. Detection SNR— A receiver model for calculating the measurement precision assumed a simplified backscatter geometry in which the Doppler shift is $2V/\lambda$. Figure 3.4.5-2 shows a schematic of this model.

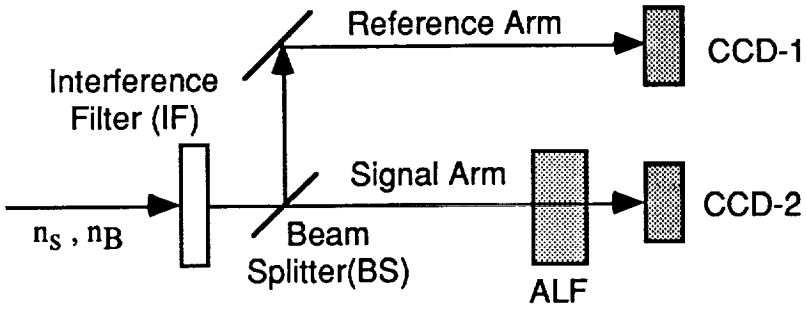

Figure 3.4.5-2 Receiver SNR Analysis Model

The velocity rms error in this case is given by:

$$(\delta V)_{rms} = (1/2)\,\lambda(\delta v)_{rms}$$

The relative error in ALF transmission measurement due to various noise sources is given by the expression below:

$$\delta T/T = (\eta_2/\eta_1)(SNR1^{-1} + SNR2^{-1})^{1/2}$$

where

$$SNR1 = (\eta_1 n_S)^2 / [\eta_1(n_S + n_B) + M^2 (n_{D1} + n_{J1}^2)]$$

and

$$SNR2 = (T\eta_2 n_S)^2 / [\eta_2(Tn_S + n_B) + M^2 (n_{D2} + n_{J2}^2)]$$

The optical train efficiencies η_1 and η_2 include the bandpass filter transmission, beam splitter reflection and transmission, CCD detector efficiency, and optical component throughput for the reference and the signal arms, respectively. The detector noise terms consist of dark current (n_D) and Johnson noise (n_J) for each CCD. The number of signal photons from laser backscatter is n_S. M is the number of camera pixels that corresponds to the linear spatial resolution in the measurement plane.

This transmission error yields an apparent spread of Doppler-shifted frequency, which in turn leads to a measurement error in velocity. Table 3.4.5-2 shows the dependence of velocity errors for different cases of noise make-up. The calculations assumed a nominal ALF transmission of 50%, bandpass filter transmission of 50%, lens/window transmission of 100%, detector efficiencies of 35%, beam splitter at 50%, and M=10.

Table 3.4.5-2 Velocity Error vs Noise Sources

n_s	n_B	$n_D + n_J^2$	δV_{rms} (m/sec)
10^5	0	0	1.23
10^5	10^6	0	5.2
10^5	0	10^7	54
10^5	0	$5x10^3$	1.7
10^6	0	0	0.4
10^6	10^6	0	0.6
10^6	10^7	0	1.6
10^6	0	10^7	5.4
10^6	0	$5x10^3$	0.4
10^6	10^6	$5x10^3$	0.65

The last entry in the table represents a possible operating point that assumes realistic conditions for noise sources. This means that the number of signal photons should be on the order of 10^6 to achieve velocity errors of less than 1m/sec.

Scatterer Density Requirement — The number density of scattering particles required to yield a given number of signal photons is calculated from an expression given by:

$$\rho_{sc} = (n_s w s_{res}^2)/[(E_L/h\nu)(d\sigma/d\Omega)(A_r/R^2)]$$

Table 3.4.5-3 lists the parameter definitions and representative values.

Table 3.4.5-3 Parameters for ρ_{sc} Calculation

n_s	Signal photon number	10^6
E_L	Laser energy/pulse	0.1 J
$h\nu$	Photon energy	$3.7x10^{-19}$
A_r	Receiver optic area	19.6 cm^2
R	Range to light-sheet	300 cm
s_{res}	Size of resolution element	1 cm
$d\sigma/d\Omega$	Differential scattering cross section	10^{-19} cm^2
ρ_{sc}	Scatterer density	$2x10^3$ cm^{-3}

This calculation indicates that an estimate for smoke particle density in section 3.4.4 exceeds the required scatterer density by an order of magnitude. Thus, existing smoke seeding is expected to provide adequate return signals.

4.0 CONCLUDING REMARKS

Under this program, we completed the calibration and error analysis of a laboratory breadboard DGV system based on a frequency-doubled Nd:YAG laser and an iodine absorption line filter (ALF). The test results showed excellent agreement between the DGV data and pitot measurements on a laminar flow jet with velocities of up to 150 m/sec. Camera electronics noise was a primary source of error; however, optimized laser light-sheet intensity and seeding levels yielded velocity data with good signal-to-noise ratios.

The survey of cameras for the next generation DGV receivers identified several commercial units with viable sensitivity and dynamic range. For some of these cameras, an electronic shutter with very short exposure capability demonstrated good skylight rejection. When combined with a narrowband filter, the shuttered cameras suppress solar background to an acceptable level.

This program also assessed the candidate lasers and absorption line filters for the flight system. We believe that Nd:host lasers and iodine ALFs represent the most mature technology for further development of DGV systems for flight measurement as well as for wind tunnel applications. Since our laboratory breadboard system already has demonstrated the pulsed Nd:YAG laser/iodine ALF approach, the next phase of DGV development can be based on a proven foundation.

Our study of a DGV system for the F-18 HARV addressed various technical issues ranging from measurement errors and signal-to-noise analysis to hardware installation considerations. From a systems standpoint, these results indicate that DGV flight measurements are feasible with appropriate modifications to the aircraft.

5.0 REFERENCES

1) H. Komine, S. J. Brosnan, A.B. Litton, and E.A. Stappaerts, "Real-Time, Doppler Global Velocimetry," 29th Aerospace Sciences Meeting (Jan. 7-10, 1991, Reno, Nevada), paper AIAA-91-0337.

2) H. Komine and S. J. Brosnan, "Instantaneous three-component, Doppler Global Velocimetry," Fourth International Conference on Laser Anemometry, Advances and Applications, (August 5-9, 1991, Clevaland, Ohio), ASME Proceedings, (eds. A. Dybbs and B. Ghorashi) Volume 1, p. 273.

3) J. F. Meyers and H. Komine, "Dopper Global Velocimetry: A New Way to Look at Velocity," Fourth International Conference on Laser Anemometry, Advances and Applications, (August 5-9, 1991, Clevaland, Ohio), ASME Proceedings, (eds. A. Dybbs and B. Ghorashi) Volume 1, p. 289.

4) J.F. Meyers, J. W. Lee, A. A. Covone, "*Three Component Doppler Global Velocimeter Measurements of the Flow Above a Delta Wing*," Sixth International Symposium on Applications of Laser Techniques to Fluid Mechanics, July 20-23, 1992, Lisbon, Portugal

5) R. B. Miles and W. Lempert, "*Flow diagnostics in unseeded air*", 28th Aerospace Sciences Meeting (Jan 8-11, 1990, Reno, Nevada) paper AIAA-90-0624

6) Technical discussions with J. F. Meyers, NASA Langley Research Center.

7) Photonics Spectra, p 103 (August, 1991)

8) Spectre Moleculaire de L'Iode Lab. Aime Cotton Orsay-France.

REPORT DOCUMENTATION PAGE

Form Approved
OMB No. 0704-0188

1. AGENCY USE ONLY *(Leave blank)*	2. REPORT DATE	3. REPORT TYPE AND DATES COVERED
	JANUARY 26, 1994	Contractor Report

4. TITLE AND SUBTITLE
Doppler Global Velocimetry - Development of a Flight Research Instrumentation System for Application to Non-Intrusive Measurements of the Flow Field

5. FUNDING NUMBERS
C NAS1-19440
WU 505-59-10-09

6. AUTHOR(S)
Hiroshi Komine, Stephen J. Brosnan, William H. Long, and Eddy A. Stappaerts

7. PERFORMING ORGANIZATION NAME(S) AND ADDRESS(ES)
Northrop Electronics Systems Division
Hawthorne Site
2301 W. 120th Street
Hawthorne, CA 90251-5032

8. PERFORMING ORGANIZATION REPORT NUMBER

9. SPONSORING / MONITORING AGENCY NAME(S) AND ADDRESS(ES)
National Aeronautics and Space Administration
Langley Research Center
Hampton, VA 23691-0001

10. SPONSORING / MONITORING AGENCY REPORT NUMBER
NASA CR-191490

11. SUPPLEMENTARY NOTES
Langley Technical Monitor: James F. Meyers
Final Report

12a. DISTRIBUTION / AVAILABILITY STATEMENT
Unclassified - Unlimited

Subject Category 35

12b. DISTRIBUTION CODE

13. ABSTRACT ***(Maximum 200 words)***

Doppler Global Velocimetry (DGV) is a new diagnostic tool for that offers potential for flow field measurements in flight by acquiring three-component velocity data in near real-time during flight maneuvers. The feasibility of implementation of a flight DGV system aboard NASA's High-Angle-of-Attack Research Vehicle (HARV) was addressed in this work be identifying the essential characteristics of a flight measurement system and by performing calibration and error tests. Results from this work were: (1) an outline that establishes a preliminary basis for system configurations by analyzing measurement errors, installation issues, and operating requirements; (2) measurement of the accuracy of the DGV technique using a laboratory breadboard DGV system based on a frequency-doubled Nd:YAG laser and iodine Absorption Line Filter (ALF), which showed excellent agreement between the DGV data and pilot measurements on a laminar flow jet with velocities of up to 150 m/sec; (3) a survey of DGV system components and technologies that are relevant to the design of a flight measurement system, including a survey of cameras for the next generation DGV receivers; (4) an assessment of the candidate lasers and absorption line filters for the flight system, resulting in a near-term recommendation of Nd:host lasers and an iodine ALF for both flight and wind tunnel applications.

14. SUBJECT TERMS
Velocimetry, DGV, Doppler, wind tunnel, flight test

15. NUMBER OF PAGES
54

16. PRICE CODE

17. SECURITY CLASSIFICATION OF REPORT	18. SECURITY CLASSIFICATION OF THIS PAGE	19. SECURITY CLASSIFICATION OF ABSTRACT	20. LIMITATION OF ABSTRACT
Unclassified	Unclassified		